

CASE FILE COPY

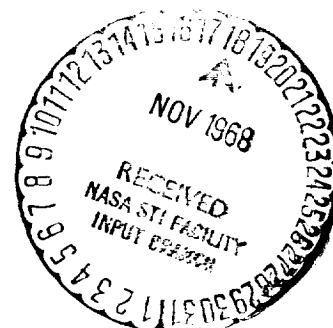
A STUDY OF CHARGED PARTICLE MOTION
IN MAGNETIC RADIATION SHIELDING FIELDS

By S. H. Levine and R. Lepper

Prepared under Contract No. NAS8-21048 by
NORTHROP CORPORATE LABORATORIES
Hawthorne, California

for

NATIONAL AERONAUTICS AND SPACE ADMINISTRATION



A STUDY OF CHARGED PARTICLE MOTION
IN MAGNETIC RADIATION SHIELDING FIELDS

By S. H. Levine and R. Lepper

Distribution of this report is provided in the
interest of information exchange. Responsibility
for the contents resides in the author or
organization that prepared it.

Prepared under Contract No. NAS8-21048 by
NORTHROP CORPORATE LABORATORIES
Hawthorne, California

for

NATIONAL AERONAUTICS AND SPACE ADMINISTRATION

FOREWORD

This document, "A Study of Charged Particle Motion in Magnetic Radiation Shielding Fields", is the final technical report prepared for the NASA George C. Marshall Space Flight Center by Northrop Corporate Laboratories, Northrop Corporation, Hawthorne, California, under contract NAS8-21048; Messrs. E. Urban and L. Lacey were technical monitors for this contract.

The work reported herein was performed under the direction of Dr. S. H. Levine, Principal Investigator, who performed most of the analyses and the writing of this report. Mr. R. Lepper was responsible for the construction and performance of the experiments in the MAGSIM.

The authors wish to thank Dr. A. Bhattacharjie for his helpful comments concerning the theoretical aspects of this program, Mr. G. Duckworth for his advice concerning the computer program, Mrs. Deloris Davis for typing the report, and Mr. W. A. Coonfield for editing it.

TABLE OF CONTENTS

	Page
SUMMARY	1
INTRODUCTION	2
ANALYTICAL DISCUSSION	5
EXPERIMENTAL PROCEDURE	9
DATA ANALYSIS AND RESULTS	27
CONCLUSION.	54
REFERENCES	61
APPENDIX.	62

A STUDY OF CHARGED PARTICLE MOTION IN MAGNETIC RADIATION SHIELDING FIELDS

By S. H. Levine and R. Lepper
Northrop Corporate Laboratories

SUMMARY

An experimental method has been effected for determining the angular flux about a point dipole magnet produced by an incident anisotropic charged particle flux. This information will be useful in optimizing active shields with material shields. The experiment was performed with the Magnetic Shield Simulator (MAGSIM), a device used to determine the shape of shielded regions produced by externally deflecting magnets. The MAGSIM was modified to provide more accurate trajectory data for this experiment.

The experimental data involve two positions of the electron gun, simulating the incident charged particle flux from two points in space (six directions if symmetry is employed). One position is in the equatorial plane of the magnet and the other is in a plane whose normal is 45° to the equatorial plane. The data are recorded when the trajectories score a fluorescent screen positioned about the point dipole. The screen itself is located in a plane defined by the pole axis of the magnet and the pivot point of the gun. Rotating the gun through all possible directions at each position provide quantitative information concerning the incident directions of the particle flux that intersect the screen as well as the angular flux data.

A computer program has been written to reduce the data and print out the results in a convenient format. The program consists of two parts; the first determines pertinent parameters concerning the trajectories as they score the screen and then punches the data needed as input to the next phase. This first set of calculations is made to assure the accuracy of the data before proceeding to the next part wherein the angular flux is determined. Although the procedure

computes the angular flux about the point dipole associated with an isotropic flux for future comparison with theoretical results, the extension of this procedure to anisotropic flux and other magnets is obvious.

Considerable data are provided for the two source positions. Extension of these methods to provide complete coverage of all points in space and other magnets is described in the conclusion.

INTRODUCTION

Magnetic shielding utilizes the concept that, in appropriate magnetic fields, regions exist wherein charged particles with momenta less than some given momentum cannot enter. This phenomenon originally was studied by Störmer¹ in connection with various cosmic-ray phenomenon in the geomagnetic field. He approximated the geomagnetic field with a magnet dipole. Theoretical and experimental studies of magnetic shielding in connection with the protection of manned and unmanned spacecraft from damaging effects of incident charged particles have been made in recent times with various systems (Levy,² Tooper,³ Bhattacharjie and Michael,⁴ Levine and Lepper⁵) by computing the totally forbidden volume. With encouraging results, the criterion of totally forbidden volume has also been used to determine feasibility of magnetic shielding systems, using superconducting magnets, by comparing with size and weight using conventional material shielding devices (Levy,² Bhattacharjie and Michael,⁴ Tooper³). One can also directly obtain, by experimentation, a sufficiently accurate estimate of the totally forbidden volume (Levine and Lepper⁶). This latter approach is considerably simpler than the theoretical approach when analyzing shielding and totally forbidden volumes in complex magnetic fields and has been used principally to study shields for protecting against artificially injected electrons. Such active shields can offer a tremendous mass advantage over material shields since they are both effective in diverting the electron with its low mass and in preventing the production of the highly penetrating bremsstrahlung.

The principal problems associated with active shields for electrons are different from those for the high energy protons. In the former, the major mass subsystem is the cryogenic cooling system and its power supply whereas with the latter, the structural mass is the heaviest component. The light mass of the electrons permits effective shields to operate with low total currents so that the self-induced forces on these magnets can be coped with using simple structural supports. Corresponding magnets for protons require currents approximately 50 times larger increasing the forces between magnets by a factor of 2500. Consequently large massive structures are needed to contain and support the superconductors.

The ampere-turn requirements for active shields used to protect against high energy protons may be reduced by various methods. Active shields designed to protect against the high energy protons in the Van Allen Belt can take advantage of the proton anisotropy and the earth's magnetic field. The spiralling motion of these protons about the earth's magnetic field, together with the forced orientation of the magnets, offer an advantage to active shields. A single current loop shield design automatically orients itself to provide protective regions in the center of the shield which greatly reduces total current requirements⁷. The region within the center of the single loop is totally forbidden to protons having momentum below the design value. Indeed, to date all active shields have been designed to provide totally forbidden volumes. The possibility of extending the vehicle volume into the partially shielded region will reduce the total weight of the active shield system for a given vehicle. A partially shielded region has the characteristic feature that charged particles having a specified set of initial directions of motion at large distances are forbidden from entering it. Theoretical analysis of partial shielding in the general case is a difficult problem, requiring extensive numerical computation, even in the point dipole field, since a knowledge of the third field integral of motion is required. However, under suitable initial conditions, it has been recently found that theoretical estimates of the effects of partial shielding can be obtained by using Liouville's theorem.

This was first achieved by Prescott, Urban, and Shelton⁸ who showed that, for spatially uniform and isotropic particle distribution at large distances, application of Liouville's theorem to cylindrically symmetric magnetic shields yields simple analytic criteria for deriving quantitative estimates of partial shielding.

Further improvement in active shield designs may be attained by determining the angular distribution of the proton flux at the surface of the vehicle, and integrating material shields to provide optimum protection.

The problem of estimating the angular distribution and the partial shielding in a given magnetic field has no simple theoretical solution to date. The theoretical approach would basically be to numerically integrate the equations of motion in order to obtain the distribution of the charged particles. This is a task of considerable magnitude. On the other hand recent advances in experimental techniques using special phosphorescent screens together with gas excitation has provided the possibility of obtaining the angular distribution. The purpose of this program has been to effect these techniques using a point dipole magnet.

In the next section, the work of Störmer¹ and Prescott, et al,⁸ is reviewed for reference and understanding of the experiments which are all performed utilizing the Magnetic Shield Simulator (MAGSIM). This is a device which has been modified in this program to improve its accuracy and permit taking the appropriate data. The MAGSIM, including the modifications and the experimental technique, is described in the third section.

In the fourth section, the data analysis and results are presented. Included in this section is a description of a FORTRAN computer program employed in the data reduction and analysis. The conclusions are given in the final section.

ANALYTICAL DISCUSSION

We shall very briefly consider the motion of a charged particle in an axially symmetric static magnetic field from shielding point of view without any derivations. The notation followed is the same as given by E. W. Urban.⁹ In an axially symmetric magnetic field described by the vector potential, $\underline{A} = A_\phi \hat{\phi}$, where ϕ is the azimuthal angle about the axis of symmetry, the equations of motion are

$$n(\ddot{\rho} - \dot{\rho}^2 \theta^2) = -\frac{1}{2} \frac{\partial}{\partial \rho} Q^2 \quad (1)$$

$$n(\rho \ddot{\theta} + 2\dot{\rho} \dot{\theta}) = -\frac{1}{2\rho} \frac{\partial}{\partial \theta} Q^2 \quad (2)$$

together with two first integrals of motion

$$n(\dot{\rho}^2 + \rho^2 \dot{\theta}^2) = 1 - Q^2 \quad (3)$$

$$-\sqrt{n} \rho \sin \phi = \frac{2\bar{\gamma}}{\rho \sin \theta} + \frac{e}{p} A_\phi = Q, \quad (4)$$

where $n = C_{st}^2/v^2$, C_{st} being the Stormer distance. For a magnetic dipole,

$$\frac{e}{p} A_\phi = \sin \theta / \rho^2. \quad (5)$$

Analysis by Stormer for the magnetic dipole case has shown the existence of inner and outer allowed regions and inner and outer forbidden regions corresponding to different values of $\bar{\gamma}$ and Q . The actual trajectory of a particular particle can be determined only by numerical integration of the equations of motion, but the trajectory, however complicated, will remain in the outer allowed region defined by the $\bar{\gamma}$ value of the particle. Stormer showed, in addition, that the particular inner forbidden region outlined by the curve $Q = 1$ which occurs at $\bar{\gamma} = -1.00$ gives the totally shielded region. Considering magnetic systems more complex than a pure dipole, Urban proved that the totally shielded region corresponds to the critical value $\bar{\gamma}_c$ of $\bar{\gamma}$ associated

with a saddle point in the Q surface at $Q = -1$. Denoting the critical saddle point values by $\bar{\gamma}_c$, ρ_c and Q_c , Urban established the following equations for determining them:

$$\begin{aligned}\frac{\partial Q}{\partial \rho} &= 0 \\ \frac{1}{\rho} \frac{\partial Q}{\partial \theta} &= 0 \\ Q &= -1 \\ \left[\frac{1}{\rho} \left(\frac{\partial^2 Q}{\partial \rho \partial \theta} \right)^2 - \frac{1}{\rho^2} \frac{\partial^2 Q}{\partial^2 \rho} \cdot \frac{\partial^2 Q}{\partial^2 \theta} \right] &> 0,\end{aligned}\tag{6}$$

at

$$\rho = \rho_c, \theta = \theta_c, \bar{\gamma} = \bar{\gamma}_c.$$

The active shield is designed to provide a totally forbidden region to enclose the vehicle. Due to the divergence characteristics of the magnetic field, the protected region for an incident isotropic flux is always in the shape of a toroid. The mass of the active shield per unit of protective volume is then determined for the configuration and compared to a material shield mass based on the same vehicle volume. This places an encumbrance on the active shield since only one trajectory is needed to define the completely protected volume. The feasibility of magnetic shielding would be further enhanced if, rather than considering totally shielded region, one could take into account the additional shielding due to forbidden regions corresponding to the actual $\bar{\gamma}$ values of the incident charged particles against which shielding is to be effected. These regions are conveniently referred to as "partially" shielded regions and have the characteristic feature that charged particles having a specified set of initial directions of motion at large distances are forbidden from entering these regions (and also having momenta less than some given momentum). A significant contribution to this problem has been made by Prescott, Urban, and Shelton.⁸ They have obtained the total particle flux $\Phi(r)$ through a point located by the position vector \underline{r} in a general axially symmetric

magnetic field incident by a spatially symmetric and isotropic charged particle flux at infinity by the application of Liouville's theorem.

Their result is

$$\begin{aligned}\Phi(\underline{r}) &= 0 \quad \text{if } Q_c \geq 1.0 \\ &= 1.0 \quad \text{if } Q_c \leq -1.0 \quad \text{or if} \\ &\quad -1 < Q_c < 1 \quad \text{and} \quad \frac{\partial Q_c}{\partial \rho} > 0 \quad \left. \vphantom{\frac{\partial Q_c}{\partial \rho}} \right\} \\ &= \frac{1 - Q_c}{2} \quad \text{if } -1 < Q_c < 1 \quad \text{and} \quad \frac{\partial Q_c}{\partial \rho} < 0,\end{aligned}\tag{7}$$

where

$$Q_c = Q \mid_{\bar{y} = \bar{y}_c}.$$

Partial shielding analyses circumvent individual trajectory analysis and thus do not incorporate or evolve the angular distribution of the flux impinging on the surface of the vehicle. A determination of the angular flux, $\Phi(r, \Omega) \Delta \Omega$, would permit optimizing the active shield together with a material shield, the latter being composed of the required structure and system equipment plus some additional material for complementing weakly shielded regions. Unfortunately numerical analysis of the trajectories required to provide this detailed information is far too costly and time consuming. Thus an experimental approach to attain these type data is of considerable significance to active shields.

The MAGSIM, described briefly in the next section, is utilized to obtain such data. Here the data are taken for individual trajectories programmed to simulate a distributed source on a spherical surface. Consequently it is necessary to transform the distributed source into an equivalent flux density. An isotropic source, $\Phi(\rho_0, \Omega)$, is simulated by homogeneously distributing the source over a sphere of radius ρ_0 according to the relation¹⁰

$$S(\rho_0, \Omega) = \mid \mu \mid \phi(\rho_0, \Omega),\tag{8}$$

where

$$\mu = \cos (\theta_g + 90^\circ) \quad (9)$$

Since the magnitude of the source strength is arbitrarily provided,

$$S(\rho_o, \Omega) = C |\mu|, \quad (10)$$

we normalize the flux so that

$$\int_0^{4\pi} S(\rho_o, \Omega) d\Omega = 1. \quad (11)$$

Substituting eqs. 8 and 10 into 11 and integrating, we obtain

$$C = \frac{1}{4\pi} \quad (12)$$

Thus the source intensity, ΔS , representing the number of particles moving in a solid angle $\Delta \Omega_g$ crossing area ΔA , is

$$\Delta S = Q(\rho_o, \Omega) \Delta \Omega_g \Delta A,$$

or

$$\Delta S = \frac{|\mu|}{4\pi} \Delta \Omega_g \Delta A. \quad (13)$$

These equations provide the basis for analyzing the data taken with the MAGSIM and are used to obtain the angular flux distribution about the magnet. The process of determining these parameters from the data is best understood by referring to the experimental setup as described in the next section.

Equation (13) corresponds to an isotropic flux at infinity. An anisotropic flux can be simulated by inserting a resulting function, $W(\Omega_g)$, into equation (13) to define the anisotropy as shown in equation (14).

$$\Delta S = \frac{W(\Omega_g) |\mu|}{4\pi} \Delta \Omega_g \Delta A \quad (14)$$

EXPERIMENTAL PROCEDURE

Stormer was the first to reduce the equations of motion, eq. 1 through 5, to a nondimensional form by introducing a new unit of length, C_{st} , referred to as the Stormer radius. This remarkable property of the equation of motion permits experiments to be performed with scaled-down models and low energy charged particles to provide accurate data for the larger magnets and higher energy charged particles. Scaled down experiments have been performed by Malmfors¹¹ to obtain information on cosmic ray trajectories using a point dipole magnet to simulate the earth's magnetic field and electrons to simulate the cosmic rays. Electron trajectories represent the motion of a positive charge in a cartesian coordinate system if the X axis is reversed.

The original devices employed to study the trajectories of high energy particles entering the earth's magnetosphere were called Stormertrons. The device we have developed at Northrop is a Stormertron that has been modified to permit studying in a quantitative fashion the shielded regions created by magnets. For this reason, the device has been called the MAGSIM. In order to obtain accurate trajectory information for determining the angular flux distribution about a dipole magnet for this program, the precision of the MAGSIM has been improved further.

Magnetic Shield Simulator

The magnetic shield simulator,⁶ Figure 1, consists essentially of a vacuum chamber, an electron gun, power supplies, degaussing coils, and the magnets with their supporting structure. The vacuum chamber is an aluminum coated steel tank, 5 ft in diameter and 10 ft in length, and capable of attaining pressures in the range of 1×10^{-6} Torr. Large coils have been properly placed in the chamber to reduce the earth's magnetic field approximately one order of magnitude, which appears to be adequate. The chamber is equipped with ports through which cameras are used to record the phenomena observed, a large observation window being available in the chamber door assembly.

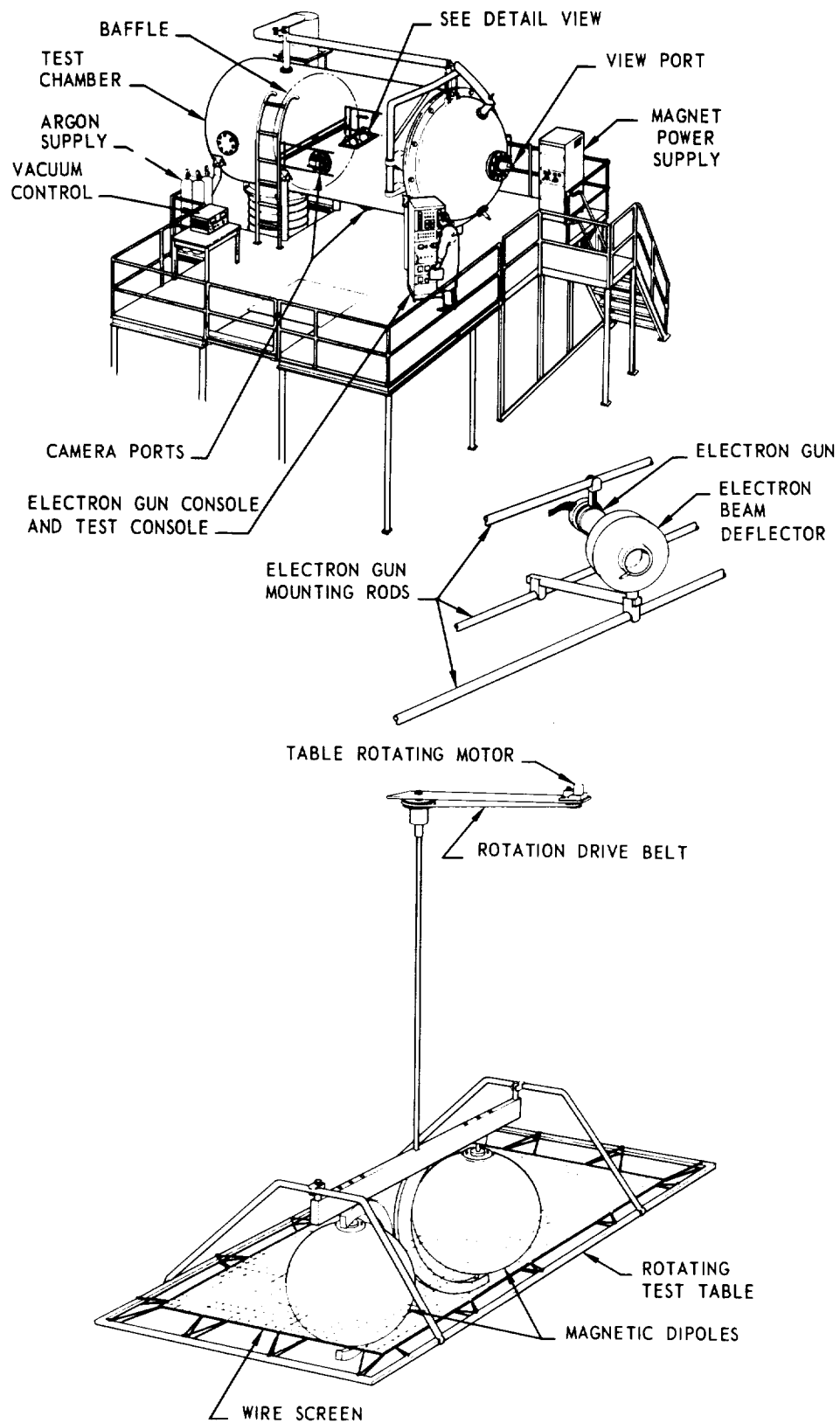


FIGURE 1 NCL MAGSIM

The hard vacuum requirement of the chamber is necessitated by the fact that the cathode of the electron source, a commercially available electron gun, must be processed in the chamber to assure adequate emission.

The magnet configuration is suspended from the top center of the chamber on a rigid structure which allows limited reorientation. Although we employed only a single-point dipole magnet in these experiments, Figure 1 shows a more complex arrangement of two such point dipoles in a general example.¹² A motor-driven pulley permits rotation of the system to present various aspects to the electron source. The center of the system is located at a point normal to each of the two data recording cameras.

Two cameras are located at ports perpendicular to each other as shown in Figure 1. The cameras and film have been selected so that adequate pictures can be obtained by backfilling the tank with argon to a pressure of 1 to 3×10^{-4} Torr. The argon atmosphere is ionized by the electron collisions. A light-blue fluorescence, rapidly photographed, defines the path of the electron streams. A grid system which allows isolating the forbidden area in any defined plane has been developed. For this the 1/2 in. mesh grid was established as optimum; the 1-in. grid did not give the detail desired and the 1/4 in. and smaller mesh sizes appeared to have an effect on the electron beam. The grid wires are coated with P-1 phosphor powder which fluoresces quite brilliantly under electron bombardment. Measurement and scaling of the photographs is accomplished by the use of an opaque projector which can be set to display the photographed objects at actual size, thus eliminating the necessity of scaling the data which improves the accuracy of the measurements.

A four-element power supply is utilized for the electron gun. Each element of the supply is a simple transformer-rectifier circuit with a 500-V, 40 mA capability. The output voltage is controlled by the use of a variac transformer at the input of each element and the main output is monitored by a digital voltmeter. With this supply it

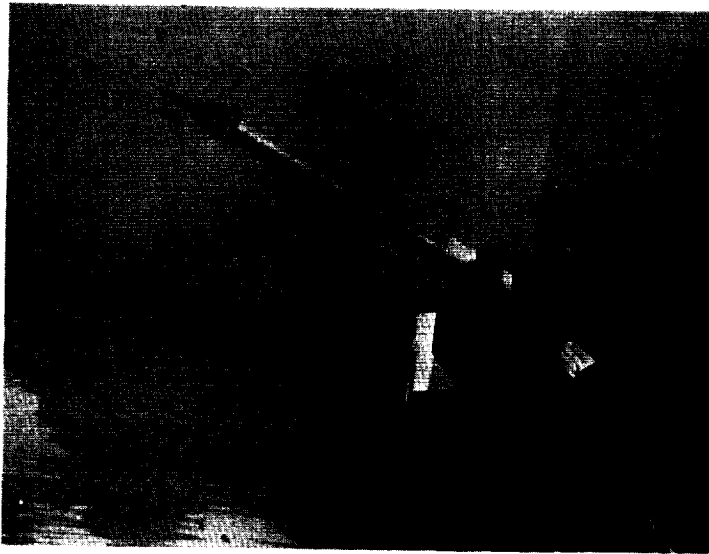
was found that the beam (discernable on the grid) could be maintained to vacuum pressures in the 10^{-8} Torr range with no difficulty. In addition to being able to rotate the magnet structure about its vertical axis to present various aspects of the magnet system to the electron source, the electron gun may also be remotely reoriented.

A new gun mount was constructed to provide accurate directional information regarding the trajectory exiting from the gun. The mount consists of a gimbal mechanism which is free to independently rotate about either of two axes. The gun may be swiveled both vertically and horizontally about one point so that the beam comes from the same point as the beam direction is changed. Each gimbal is connected to multi-turn potentiometer to provide position readout on a digital voltmeter.

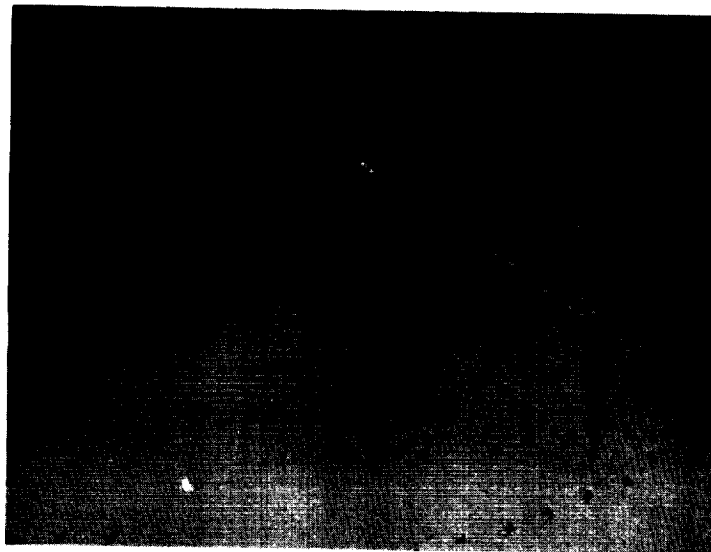
The gimbal system is designed to read out the (θ, ϕ) angles of spherical coordinates directly. Figure 2 shows this gun mount being calibrated about both angles of deflection and Figures 3 and 4 show the resultant calibration curves appropriately labeled.

For the data to be reliable, the earth's magnetic field inside the vacuum chamber must be made sufficiently small so as not to perturb the beam trajectory. Assurance that this condition was met at all times was made by remotely directing the beam at several points about the magnet (with zero current) toward fluorescent cross wires as shown in Figure 5, for which exact angles from gun pivot point are known. Precision 6-minute bubble levels were utilized to check the mount in both axes. Correlation between readout angle and actual angle to several of the cross wires was made prior to each day's run. An example of such data is shown in Table 1. It was impossible to align the gimbal system to give the exact angle; some offset in the zero position exists which remains constant for all measurements taken over an extended period of time (~ 4 weeks for the first setup). Thus we determine θ_g and ϕ_g from the relations

$$\begin{aligned}\theta_g &= C_0 + C_1 V(I) + D_2 \\ \phi_g &= B_0 + B_1 H(I) + D_1\end{aligned}\tag{15}$$



VERTICAL PLANE



HORIZONTAL PLANE

Figure 2. Calibration of electron gun mount

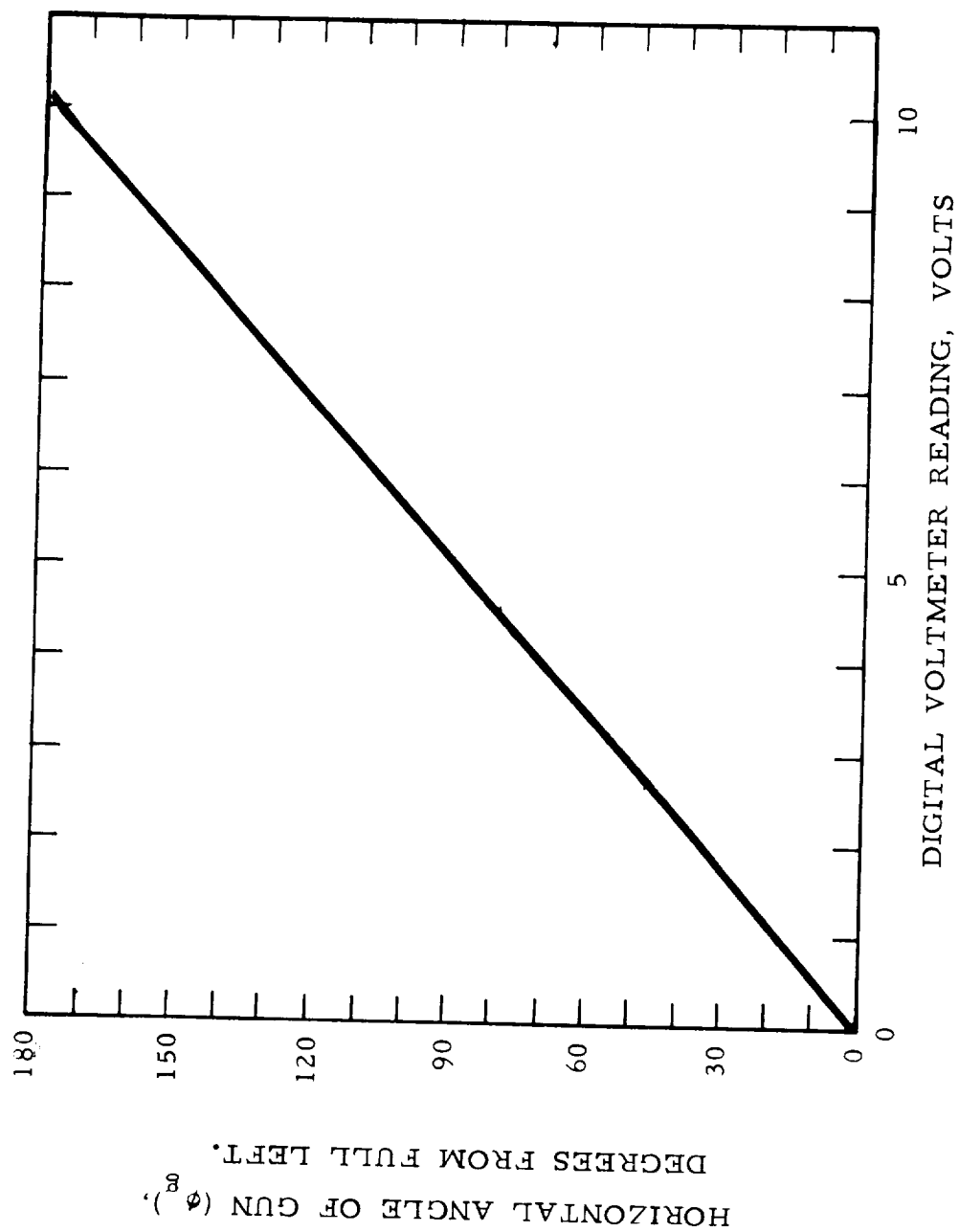


Figure 3. Calibration of gun angle indicator, horizontal.

VERTICAL ANGLE OF GUN (θ_g), DEGREES FROM FULL DOWN

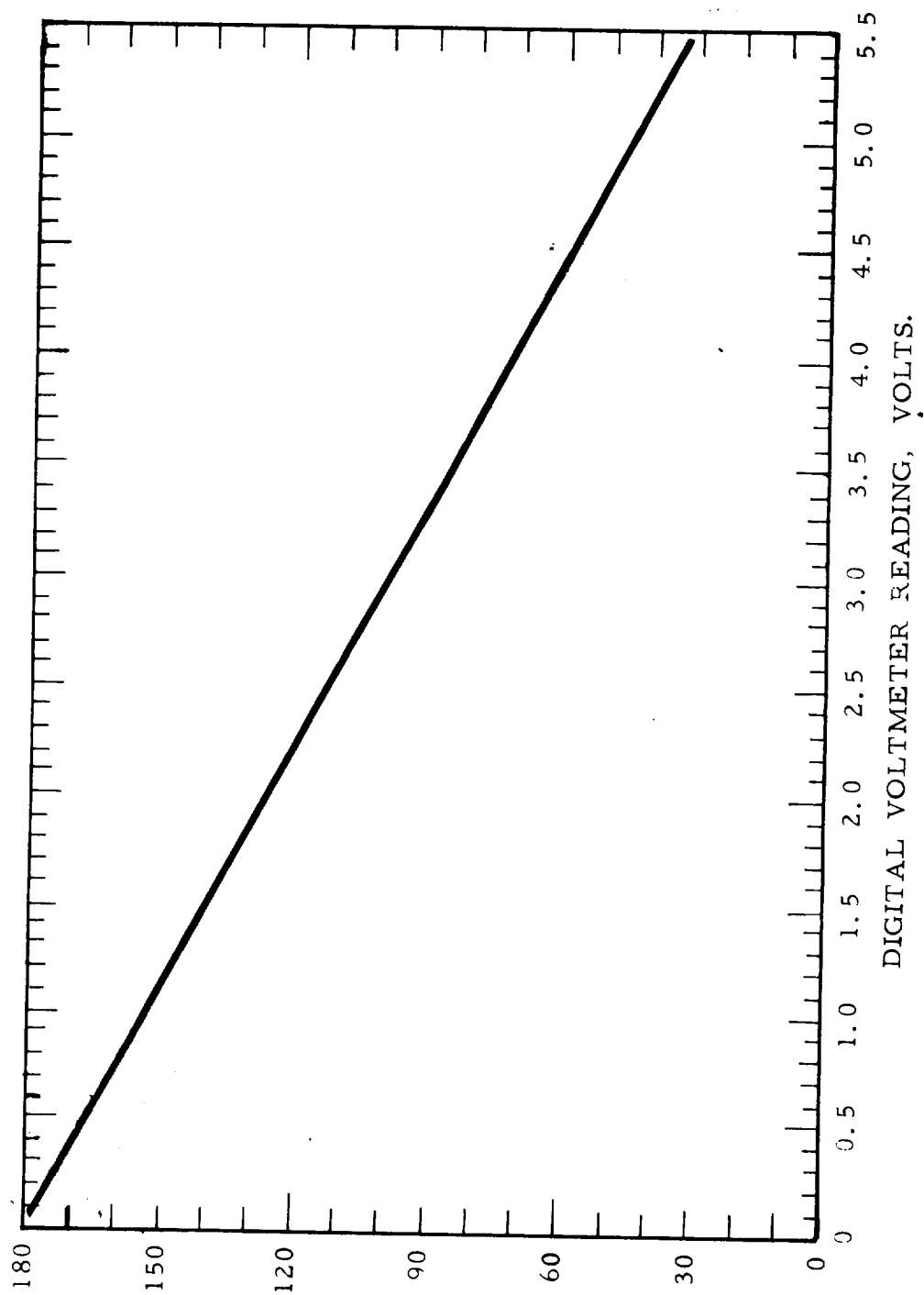


Figure 4. Calibration of gun angle indicator, vertical.

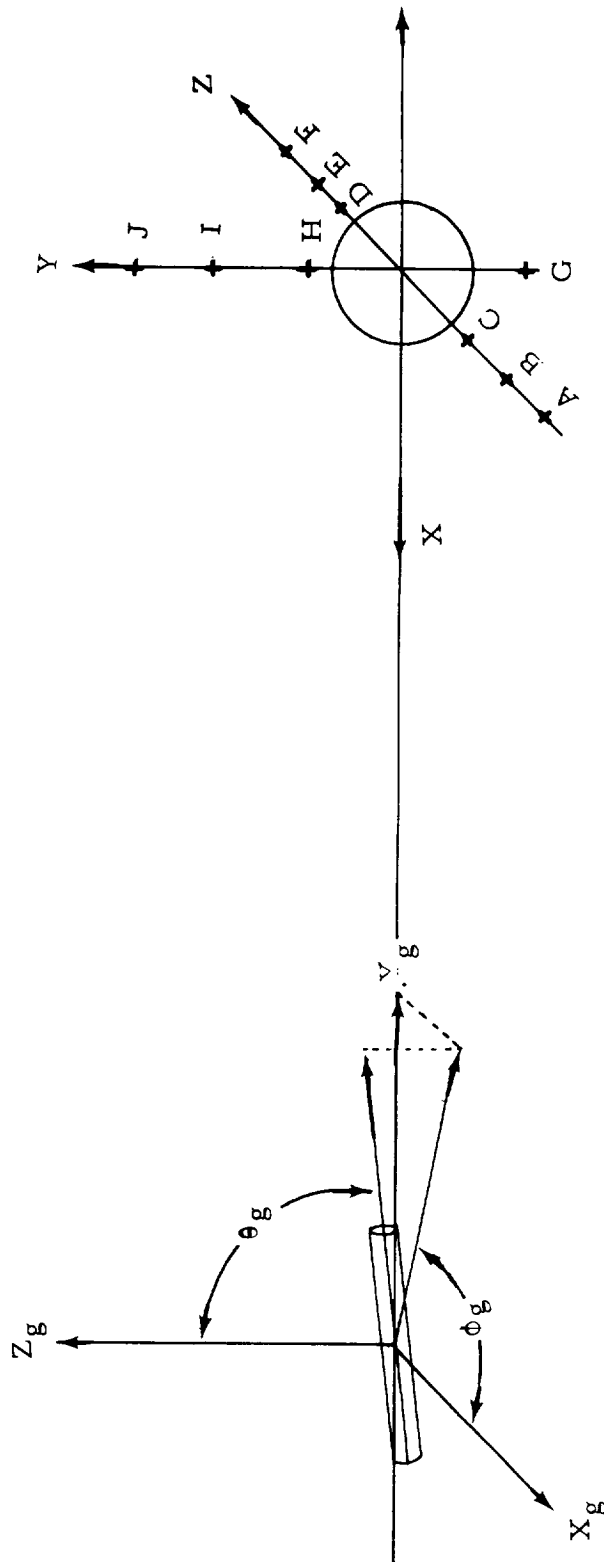


Figure 5. Calibration check points.

TABLE 1. CALIBRATION OF GUN READOUT ANGLES

Point on Figure 5	Angle as Measured using Geometric Dimensions	Angle as Measured with Gun	Diff.
A	55.150	60.25	5.10
B	66.75	69.82	3.07
C	76.80	80.23	3.43
D	96.10	99.07	2.97
E	107.10	110.08	2.98
F	117.90	119.02	1.12
*I	104.9	114.47	-.43
J	116.7	116.66	.04

Averaging B, C, D, and E gives $D_1 = 3.11^\circ$

Averaging I and J gives $D_2 = -0.22^\circ$

where C_0 , C_1 , B_0 and B_1 are constants established from the calibration curves of Figure 3 and $V(I)$ and $H(I)$ are the digital voltmeter readings. The other constants D_1 and D_2 account for the offset in alignment. Initially, two slopes were required to fit the calibration data so that the computer program used to determine ϕ and θ provides for an extra set of constants (see Appendix A). However, the final system which contains linear potentiometers produces a straight line curve with one slope.

When the point dipole is energized, it sets up a magnetic field which images in the steel vacuum chamber. Consequently, measurements of the magnetic field were made to observe the point dipole behavior of the magnet for these experiments and to provide a calibration of the point dipole, i. e., the magnetic field produced by a point dipole magnet should follow a $1/r^3$ relationship.

The point dipole magnet was mounted in the center of the vacuum tank with its center at the same height as the pivot point of the gun mount's gimbal system and with its dipole axis perpendicular to the longitudinal axis of the tank as shown in Figure 6. The magnetic field measured along the south pole and north pole axis with 1.2 A in the magnet are shown in Figures 7 and 8 respectively, together with a curve of the calculated value. The dipole moment, M , used to compute the magnetic field was

$$M = 24.8 i \text{ A-m}^2 \quad (16)$$

where i is the dipole current in amperes ($i = 1.2 \text{ A}$ for these figures). This is to be compared with $M = 24.7 i$ reported in reference 6. Magnetic field measurements along the X axis in the direction of the gun and along the Y axis in the negative (down) direction are given in Figures 9 and 10. The position of the point dipole was determined rather precisely ($\pm 0.1 \text{ cm}$), utilizing the symmetrical nature of the magnetic field and was found to lie on the pole axis displaced 0.35 cm from the geometric center toward the north pole.

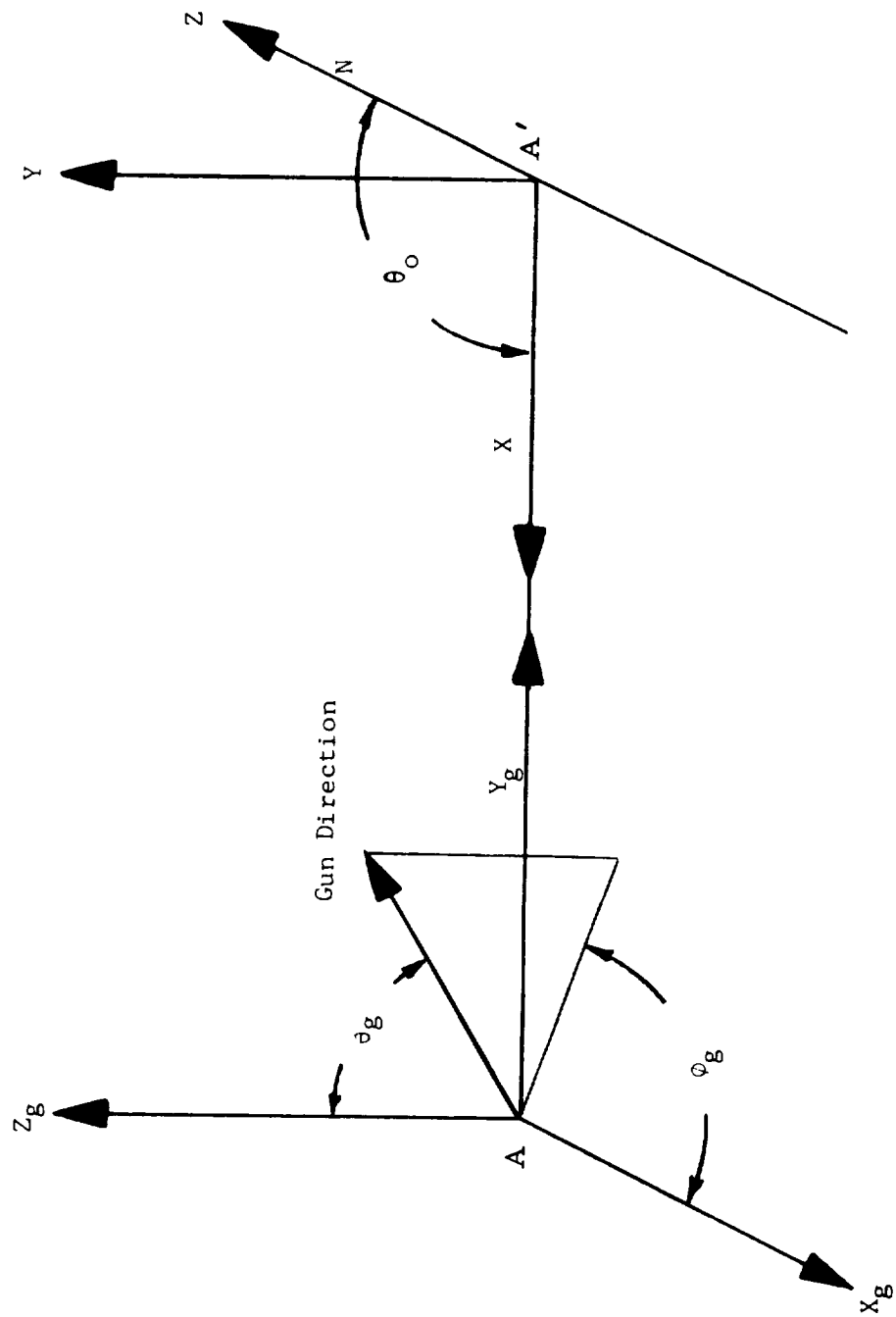


Figure 6. Coordinate system schematic.

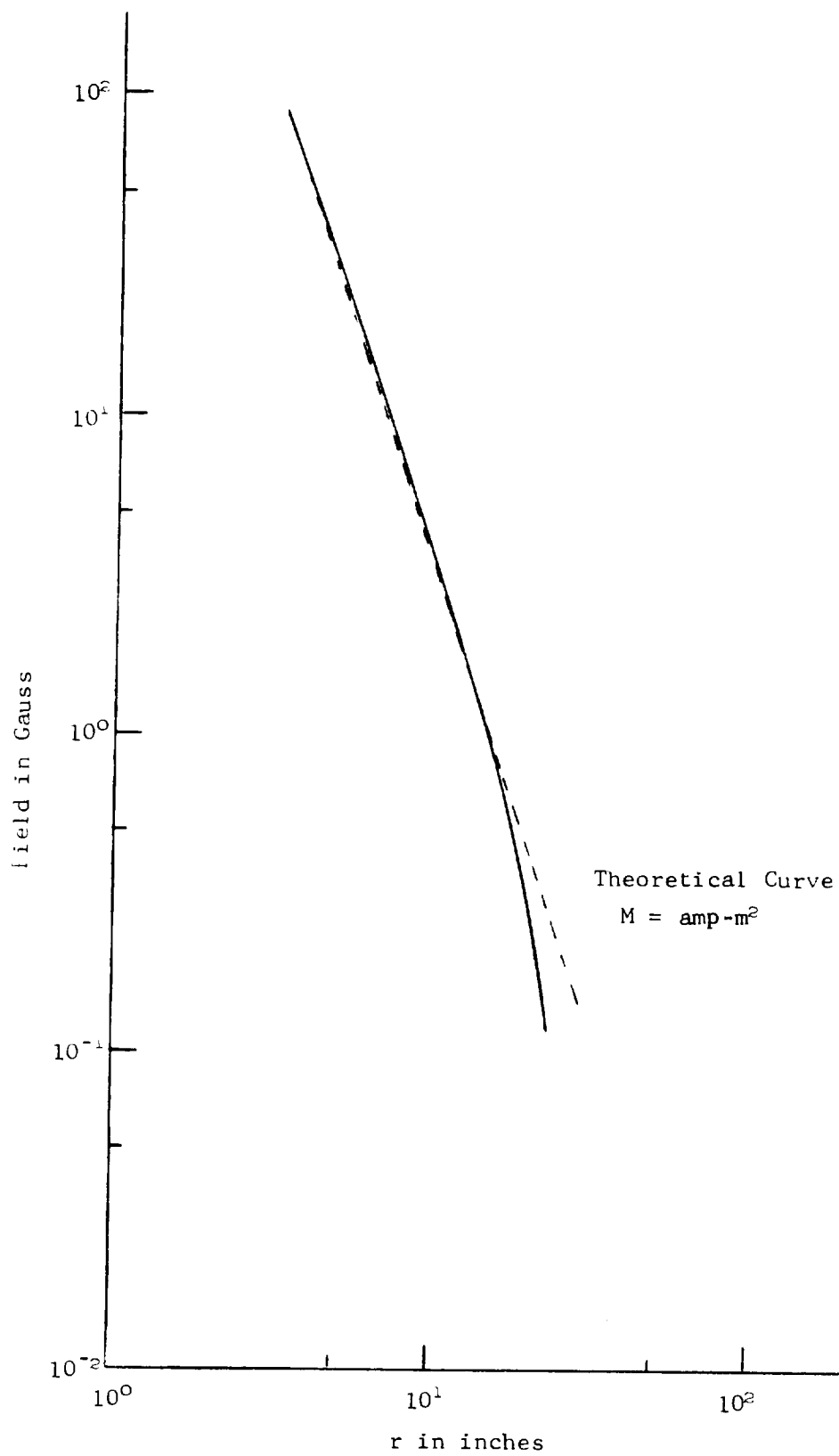


Figure 7. Dipole magnetic field in vacuum chamber from south pole to side of chamber.

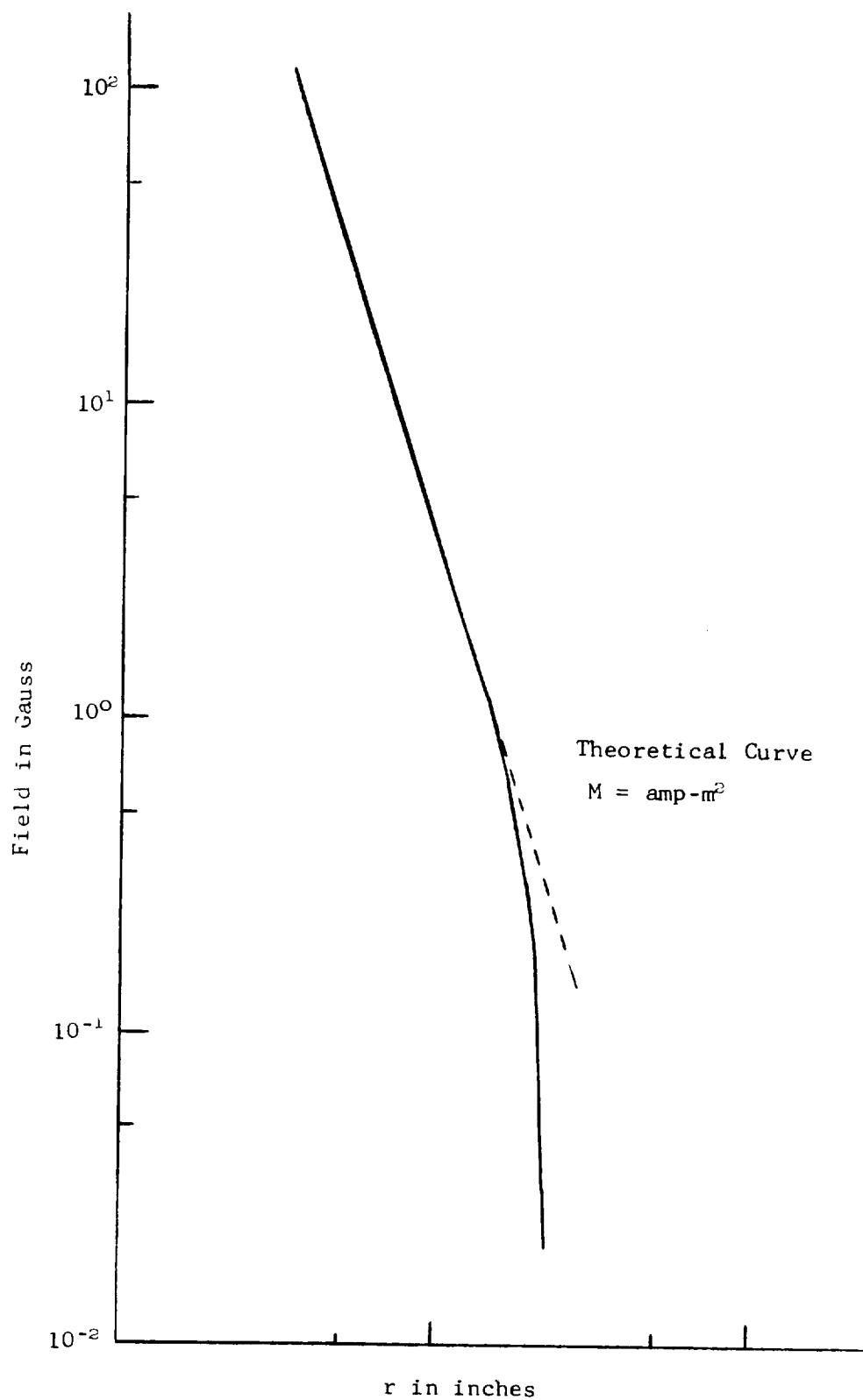


Figure 8. Dipole magnetic field in vacuum chamber from north pole to side of chamber.

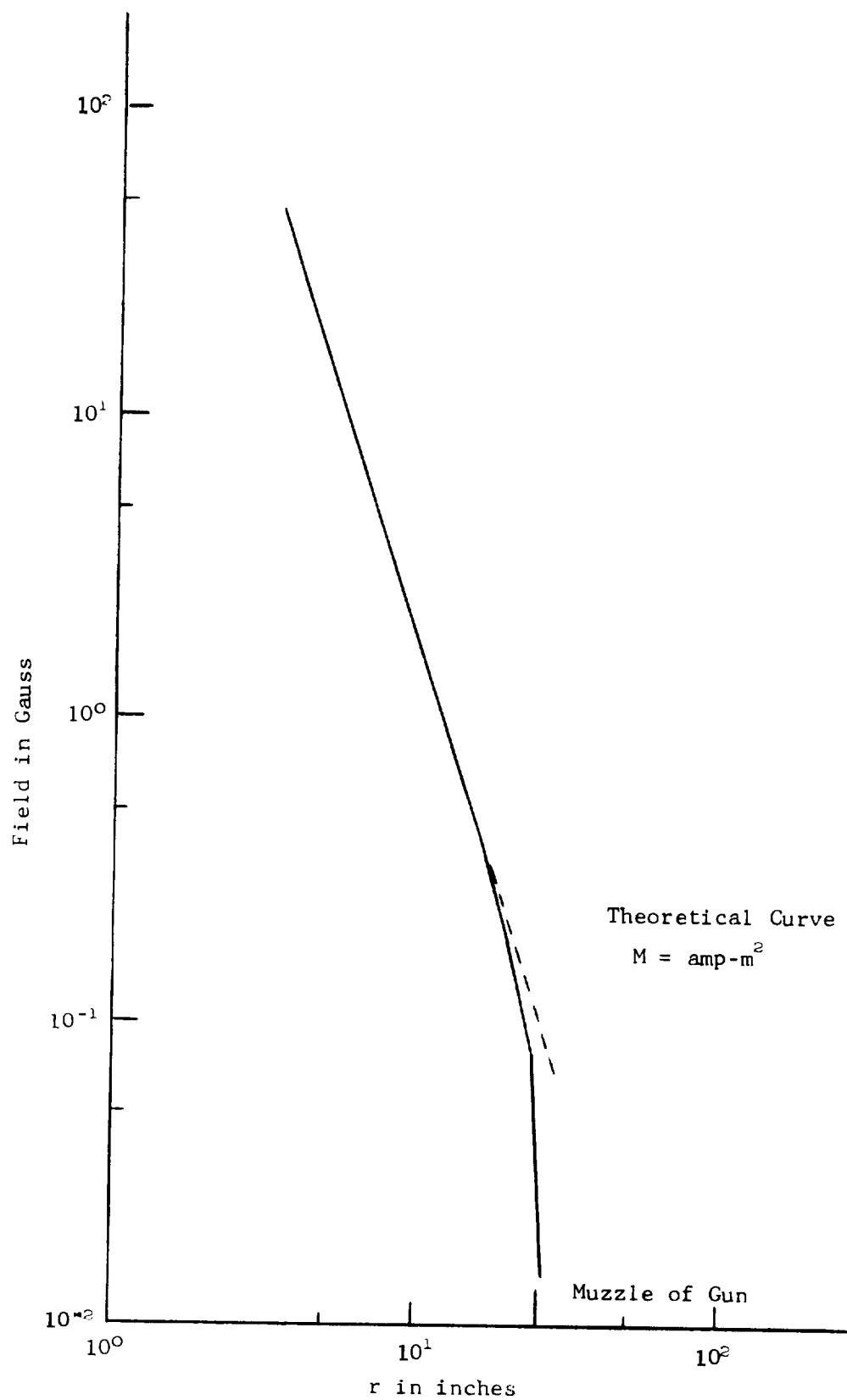


Figure 9. Dipole magnetic field in vacuum chamber from rear surface of dipole to muzzle of electron gun.

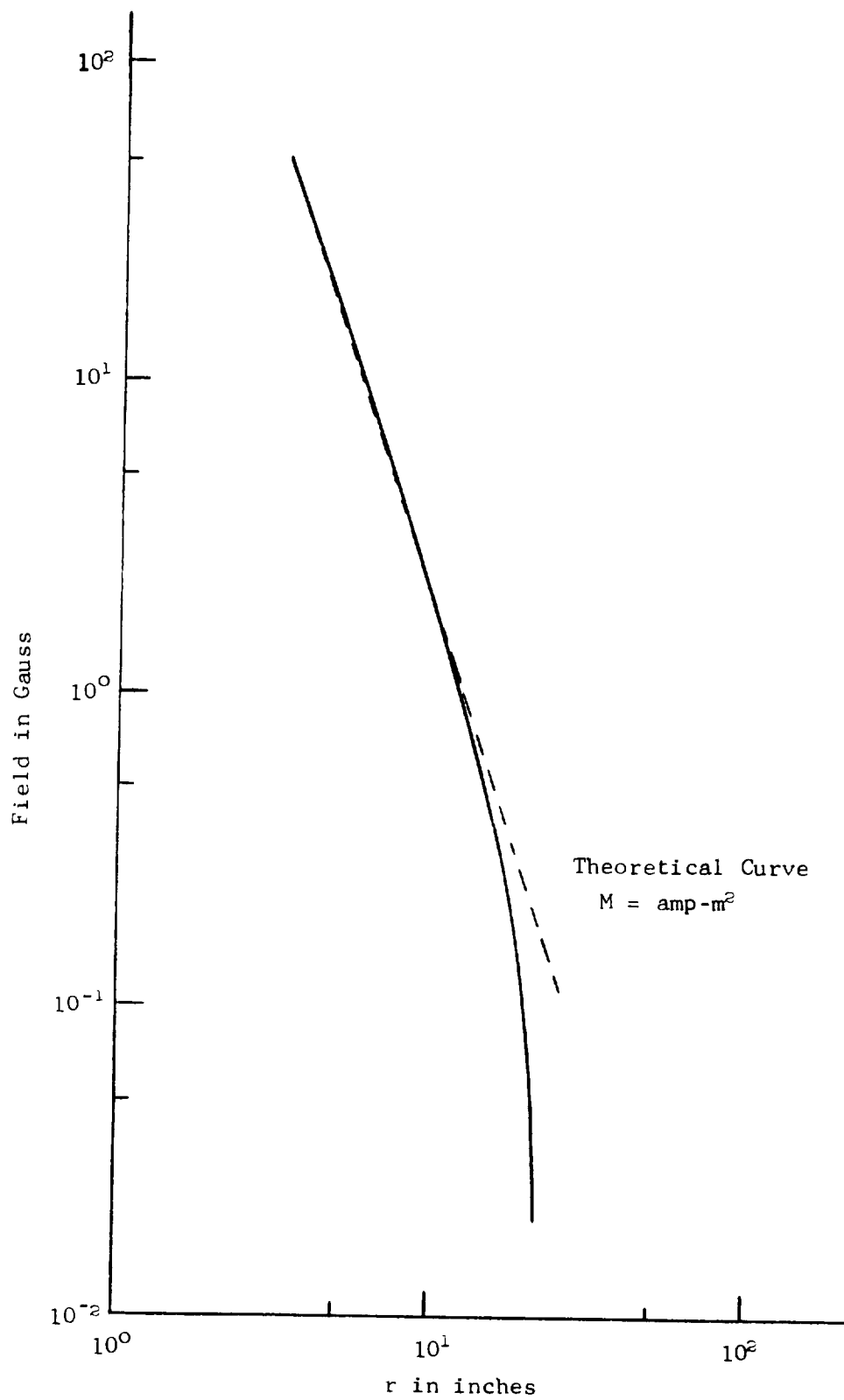


Figure 10. Dipole magnetic field in vacuum chamber from bottom surface of dipole to bottom of chamber.

It can be observed that in all cases the magnetic field drops below the anticipated value as the tank walls are approached; however, these regions are sufficiently remote from the magnet that when a charged particle enters this region it will continue to infinity. This is true except for when the beam first leaves the gun until it is within approximately 40 to 45 cm of the center of the dipole magnet. This should have only a slight effect on the assigned incident angular parameters, an effect which can be determined theoretically or experimentally.¹¹

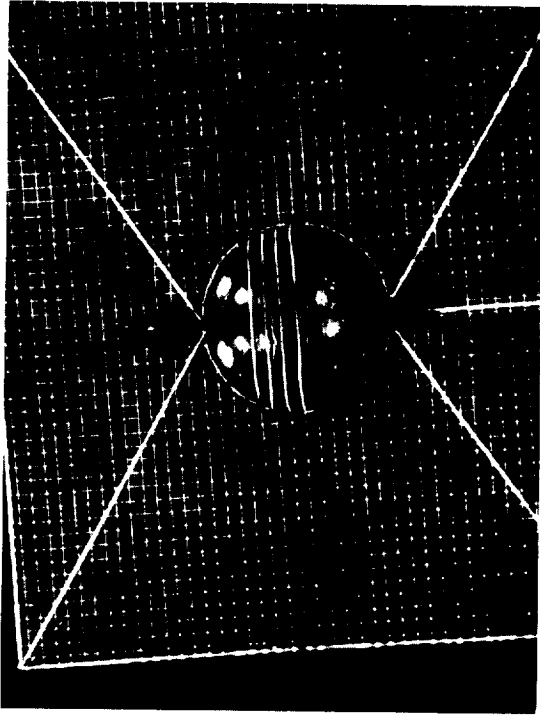
In addition to the gun angular read out being connected to a digital voltmeter, the magnet current power supply voltage was also monitored by the digital voltmeter.

Both the screen and gas excitation were used to completely define the trajectory parameters at the point where the trajectory intersected the screen. In this procedure three photographs were taken to obtain a complete set of data for one trajectory. The side and bottom cameras are used simultaneously to obtain pictures of the trajectory when gas is in the chamber from two orthogonal directions as shown in Figure 11. Another very short time exposure picture is taken with the bottom camera to help identify more precisely where the most intensive part of the beam intersected the screen, also shown in Figure 11. A photograph of the screen with lights on as seen by the bottom camera is included in Figure 11, since this picture is needed as a reference for all of the data taken with the dipole in its present orientation, i. e., $\theta_0 = 90^\circ$.

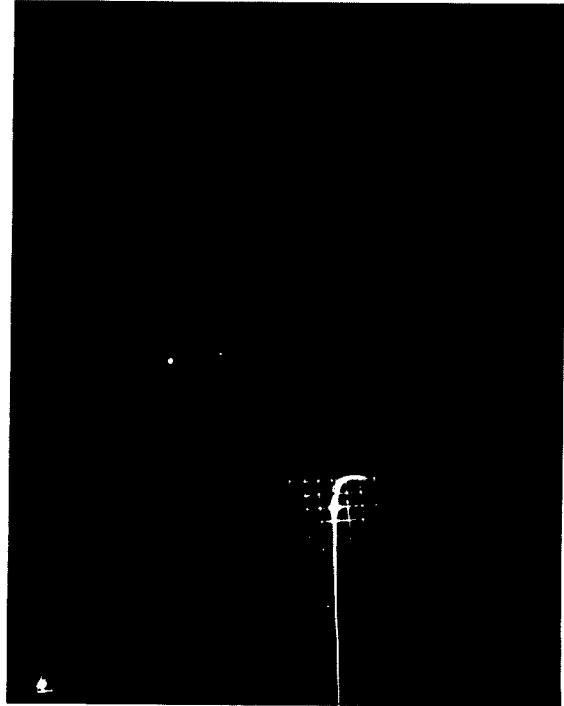
A current of 1.2 A was used in all of the point dipole experiments since this is the lowest current for which the forbidden region is just visible outside of the sphere when the electron beam voltage is 350 V. An electron beam voltage of $V = 350$ V was selected as optimum to minimize the effect of the residual field and still permit operating with a relatively low current in the magnet. Even at 1.2 A in the dipole magnet, the magnet becomes excessively hot after operating for a few hours continuously. The Stormer radius computed for the 350 electron volts and 1.2 A in the magnet is 21.73 cm (8.56 in.). According to



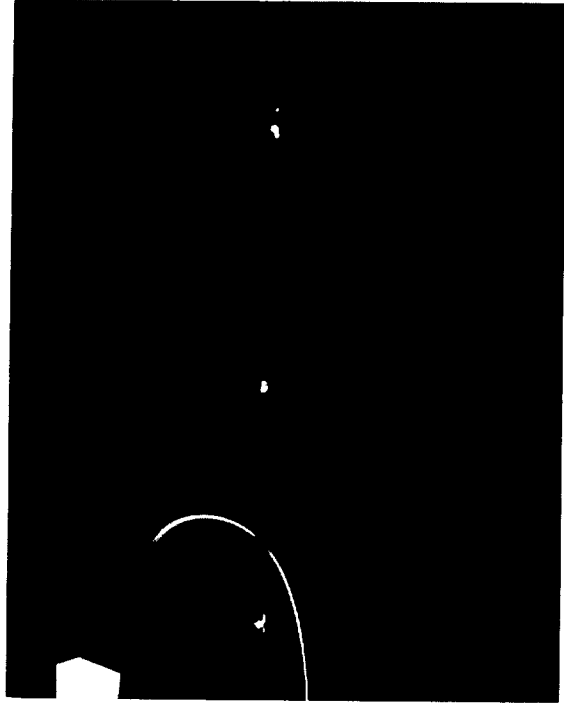
Short Exposure



Lights On



Bottom View Trajectory



Side View Trajectory

Figure 11. Data pictures from MAGSIM

Prescott et al,⁸ the flux intensity outside a Stormer unit should be unaffected by the magnet if the incident source at infinity is isotropic and spatially uniform, neglecting the shadow effect. For this reason a new 22- by 24-inch fluorescent screen was used which is well over a Stormer unit (su) in dimension and almost completely covers the field of view of the camera. Very small pin-lights were placed in the screen to key the data from one picture to another and to aid in reducing the data. An additional pair of pin lights are connected into the magnet power system to identify the south pole of the magnet; an extremely helpful aid in keeping the data in order.

As a final check on the system prior to its use each day, the gun was set at a predetermined orientation, by use of the voltage indicators, and test pictures taken. These pictures were taken each day under as near identical conditions as possible and then compared to the previous test pictures for reproducibility. Both the configuration of the trajectory and the point of impact on the screen were compared. Any change in these pictures from the previous test shots was cause for a complete review of the system including dipole current, compensating coil currents, gun orientation, gun electrical configuration, etc. since all of these contributed to the trajectory configuration. When no misadjustment was determined to be the cause of the variation of the trajectory the system was completely recalibrated.

DATA ANALYSIS AND RESULTS

Data were taken with the screen in a plane parallel to the floor and oriented at two angles, $\theta = 90^\circ$ and $\theta = 45^\circ$ to represent two incident directions of the charged particle flux. The referenced data are the two-gun angle directions, θ_g and ϕ_g , and the three sets of pictures for each trajectory. A few pictures with lights on (See Figure 11) were taken for each of the two screen angles, θ , as a reference for properly defining the XZ axis on the data pictures. To expedite the experiment and conserve film, a scan was made with the gun in the $\theta_g \phi_g$ plane to identify the angular positions of the gun that produce trajectories which either score the screen or the point dipole. Figures 12 and 13 show such scan for the θ equal 90° and 45° screen orientations respectively.

The data pictures permit determining, by two independent methods, the parameter $Q_1 = \cos \alpha_1$ at the point of the trajectory where it intersects the screen. The two separate methods for computing Q_1 at the screen provide an excellent method for validating the data and insuring the accuracy of the procedure. The first method utilizes the trajectory traces, recorded by the two cameras, to construct the velocity vector. Each photograph records a trace of the trajectory as it passes through the screen, and the tangents to these traces at the point of intersection with the screen provide sufficient information to construct \underline{v} and consequently determine Q_1 .

Since $Q_1 = \cos \alpha_1$ which, according to our nomenclature, is v_y/v where

$$\underline{v} = \underline{i} v_x + \underline{j} v_y + \underline{k} v_z, \quad (17)$$

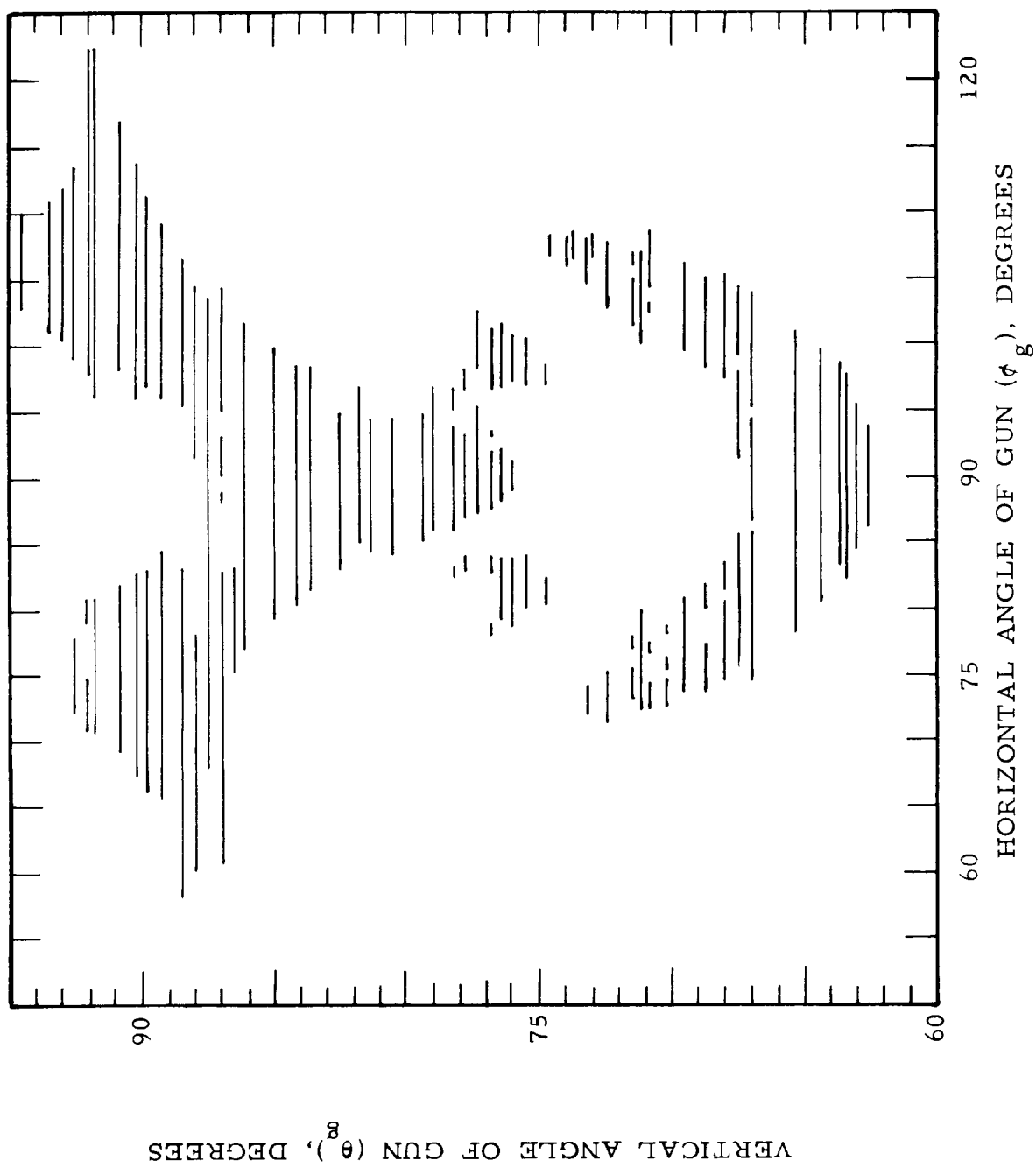


Figure 12. Scan of gun trajectories producing scores on screen or dipole with $\theta = 90^\circ$.

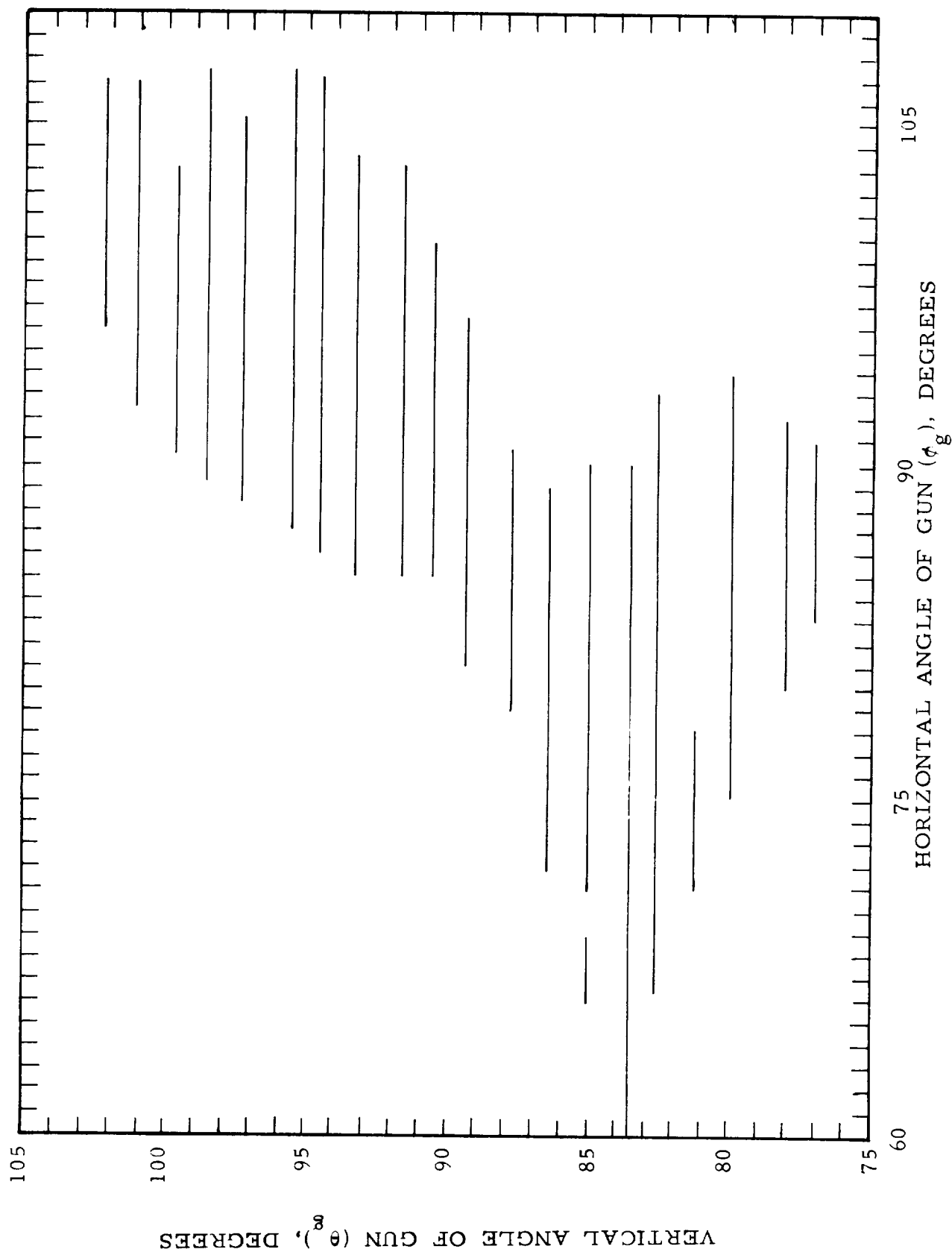


Figure 13. Scan of gun trajectories producing scores on screen or dipole with $\theta = 45^\circ$

then

$$Q = \frac{v_y}{v} = \left[1 + \frac{v_x^2}{v_y^2} + \frac{v_z^2}{v_y^2} \right]^{-1/2} \quad (18)$$

The components $\frac{v_x}{v_y}$ and $\frac{v_z}{v_y}$ are determined from the photographs of the trajectory. It is more convenient to write eq. 18 as

$$v_y = Q = \left[1 + \frac{v_x^2}{v_y^2} + \frac{v_z}{v_x} \cdot \frac{v_x^2}{v_y^2} \right]^{-1/2}, \quad (19)$$

since v_x/v_y and v_z/v_x are closer to the measured quantities.

The two cameras are located on axes perpendicular to the line, AA', of Figure 6. One camera is directly beneath the screen (View 1) and the other views the edge of the screen (View 2). The lower camera, View 1, records the trace in the XZ plane as long as the screen remains in the horizontal plane. Since this was the case for the two screen positions ($\theta = 45^\circ$ and $\theta = 90^\circ$) used in this experiment, it was possible to measure both $\tan \theta_{zx}$ or $\tan \theta_{z'x'}$ where

$$\tan \theta_{zx} = v_z/v_x \quad (20)$$

and

$$\tan \theta_{z'x'} = v_z'/v_x', \quad (21)$$

as shown in Figure 14. (The prime refers to the axes for the $\theta = 90^\circ$ which are also the axes associated with the camera.)

The side camera (View 2) data are easily interpreted for both cases if

$$\tan \theta_{y'x'} = v_y'/v_x' \quad (22)$$

is used together with $\tan \theta_{z'x'}$; otherwise

$$\tan \theta_{yx} = v_y/v_x \quad (23)$$

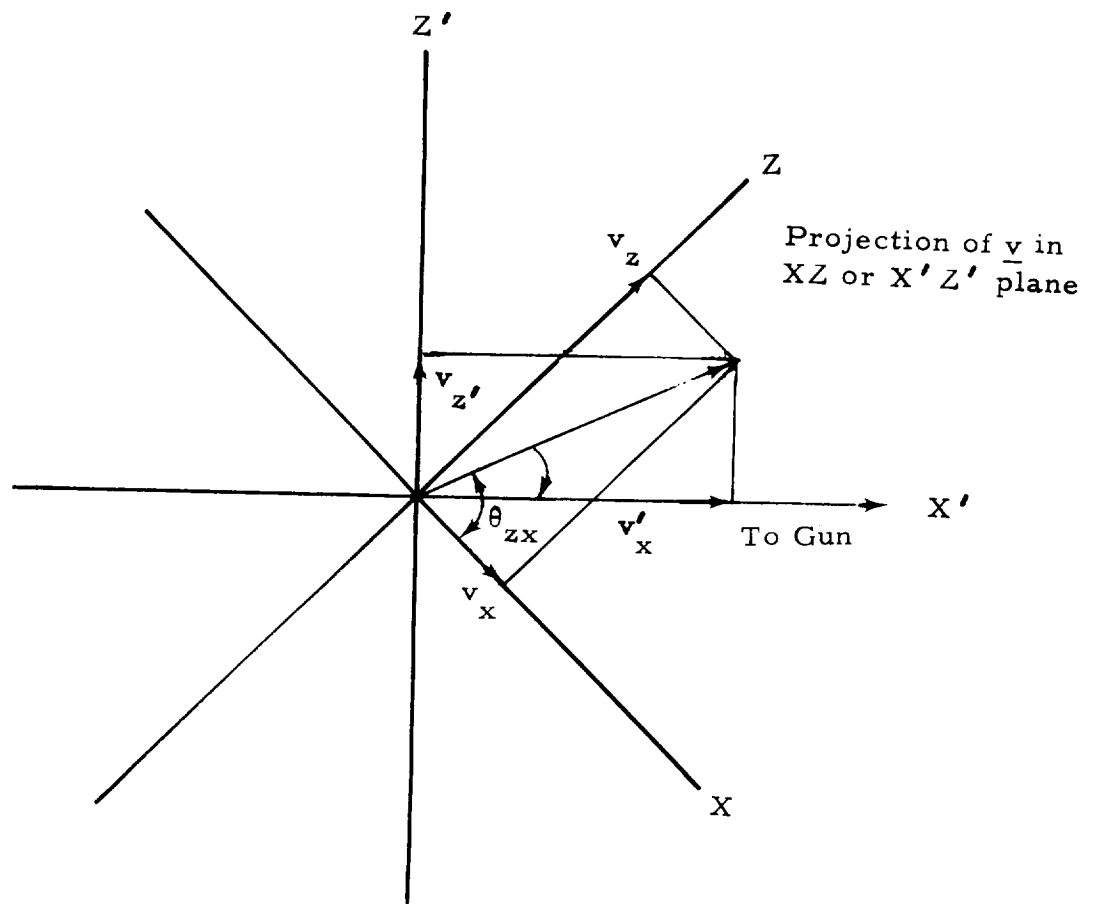


Figure 14. Bottom view as seen by camera.

must be derived. The bottom view permits determining either θ_{zx} or $\theta_{z'x'}$ since in this plane the axes can be projected on the screen; however, the side view measures v_y'/v_x' only.

It is best to use measured values of the angles $\theta_{z'x'}$ and $\theta_{y'x'}$ for determining the best value of Q_1 , since errors are minimized. $\tan \theta_{yx}$ can be derived using standard vector analysis procedures relevant to rotating the axes of the coordinate system.

Now, before rotating the axes,

$$\underline{v} = \underline{i}' v_x' + \underline{j}' v_y' + \underline{k}' v_z', \quad (24)$$

and after rotation eq. 17 represents \underline{v} ; that is

$$\underline{v} = \underline{i} v_x + \underline{j} v_y + \underline{k} v_z.$$

Since the rotation is about the y axis through an angle θ' , $\underline{j} = \underline{j}'$ and $v_y = v_y'$. Therefore

$$\tan \theta_{xy} = \tan \theta_{xy}' = \frac{v_x}{v_y} = \frac{v_x}{v_y'}, \quad (25)$$

$$\begin{aligned} v_x' &= \underline{i}' \cdot \underline{v} = \underline{i}' \cdot \underline{i} v_x + \underline{i}' \cdot \underline{k} v_z \\ &= v_x \cos \theta' + v_z \sin \theta' \\ &= v_x \cos (90 - \theta) + v_z \cos \theta, \end{aligned}$$

where $\theta = 45^\circ$. Solving for v_x/v_y , we find

$$\frac{v_x}{v_y} = \frac{\text{ctn } \theta_{yx}'}{\cos (90 - \theta) + \tan \theta_{zx} \cos \theta},$$

or

$$\frac{v_x}{v_y} = \frac{\text{ctn } \theta_{yx}'}{\cos 45 (1 + \tan \theta_{zx})}. \quad (26)$$

A singularity occurs at $\tan \theta_{zx} \cong -1.0$, introducing large errors into the results; therefore, this procedure is not utilized. That is, eqs. 21 and 22 are used in eq. 19 to determine v_y .

The second method computes Q_1 for the point dipole using eq. 4;

$$Q_1 = \frac{\sin \theta_1}{\rho_1} + \frac{2 \bar{\gamma}}{\rho_1 \sin \theta_1} , \quad (27)$$

where ρ_1 and θ_1 are the cylindrical coordinates for the position of the trajectory at the screen. The value for $\bar{\gamma}$ is obtained from the electron gun's (ρ_0, θ_0) and θ_g angular positions. Rearranging eq. 27, we obtain

$$\bar{\gamma} = \frac{1}{2} \rho_0 \left[\cos \alpha_0 \sin \theta_0 - \frac{\sin^2 \theta_0}{\rho_0} \right] , \quad (28)$$

where ρ_0 and θ_0 now refer to the trajectory coordinates at the electron gun, i. e., pivot point for the gimbals; using the right-hand coordinate system,

$$\alpha_0 = 180 - \theta_g . \quad (29)$$

Reversing the direction of the point dipole gives (see eq. 14)

$$\alpha_0 = \theta_g . \quad (30)$$

A computer program was written in FORTRAN 4 to determine Q_1 by both methods. The program prints out v_y and Q_1 where the v_y refers to eq. 19 and Q_1 refers to eq. 27. The measured raw data for each trajectory which includes the voltages corresponding to the horizontal and vertical gun angles (ϕ_g and θ_g respectively) and the $r_1, \theta_1, \theta_{y'x'}, \theta_{z'x'},$ and θ_{zx} are recorded on IBM cards together with the number assigned to the trajectory. The computer program also prints out other parameters convenient to study the major aspects of this phase of the data analysis. It is particularly useful to identify errors in the data or the analysis itself. Additionally, the computer program punches out a new set of data cards to be used with the next phase of the data analysis. These cards contain trajectory data to compute the angular flux $\Phi(\underline{r}, \underline{\Omega}) d\Omega$, a computation performed by the second phase of the computer program. A complete description of the computer program is described in the appendix.

The data is taken by moving the gun in angular steps to trace out a square in the $\theta_g \phi_g$ plane as shown in Figures 15 and 16 for the $\theta = 90^\circ$ and 45° dipole configurations respectively. This permits

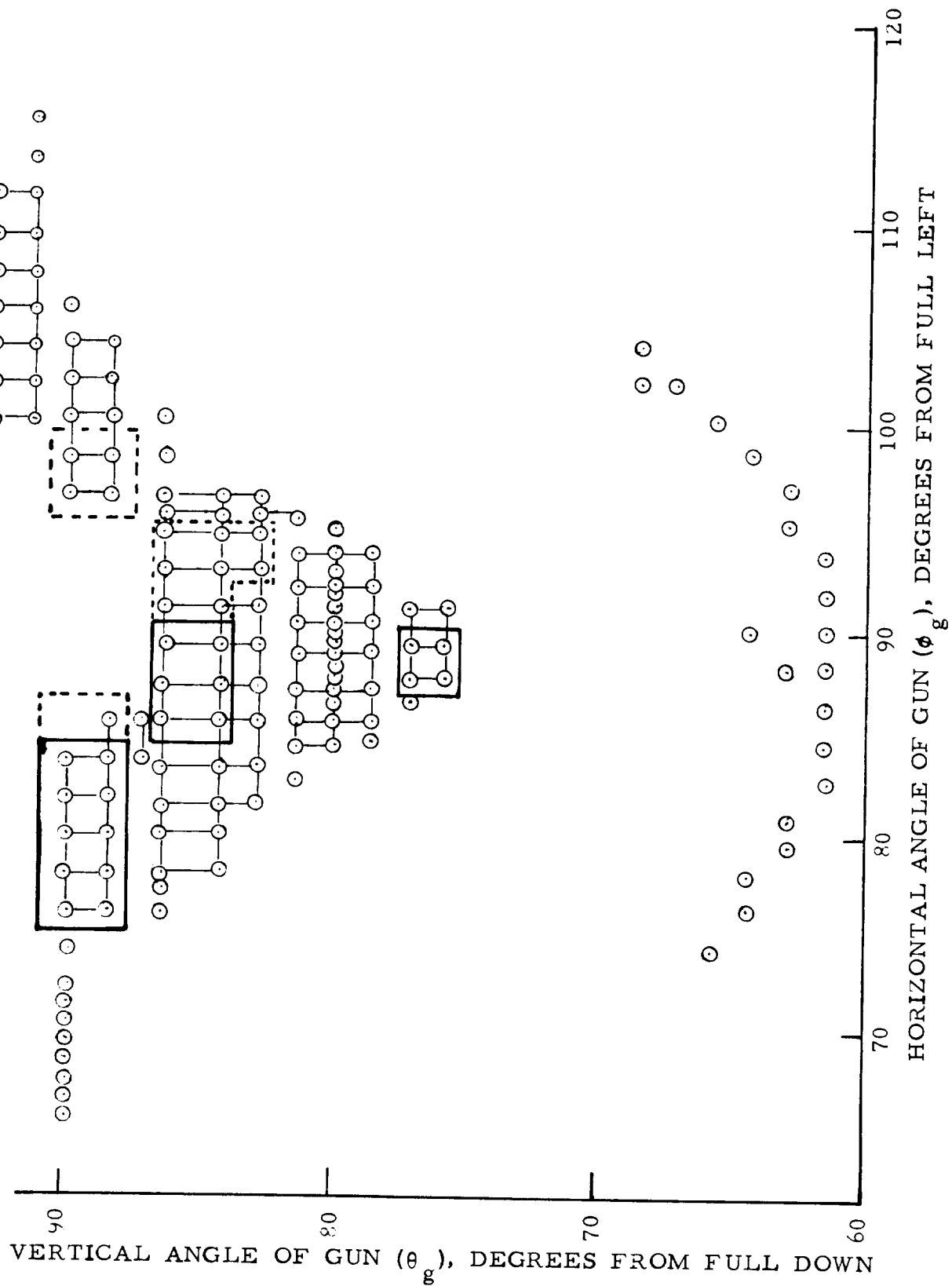


Figure 15. Electron gun angular positions for which trajectory scores the screen ($\theta = 90^\circ$).

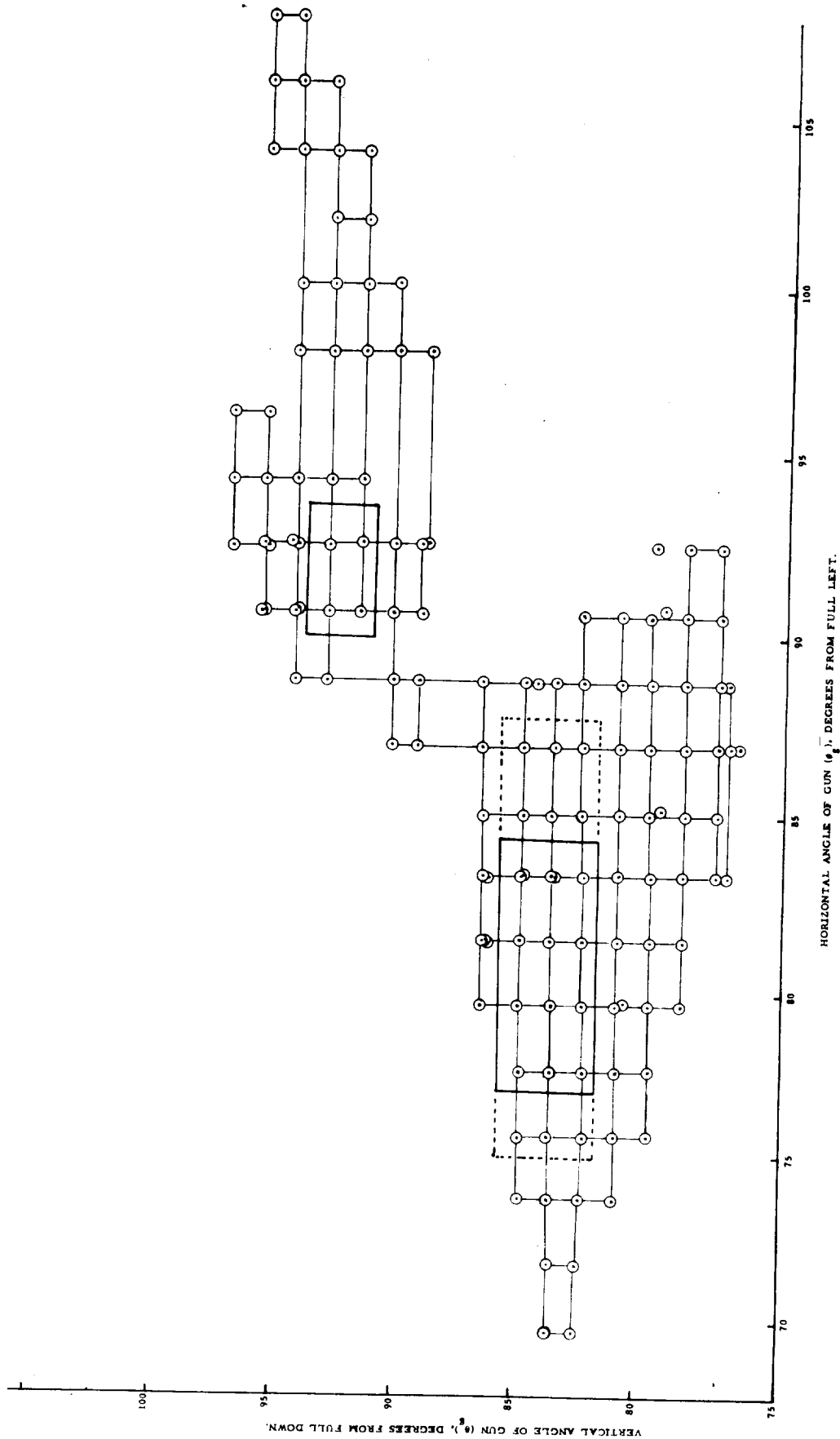


Figure 16. Electron gun angular positions for which trajectory scores the screen ($\theta = 45^\circ$).

assigning a solid angle, $\Delta \Omega_g$, with each set of four trajectories, so that the source, ΔS of equation (13), can be evaluated. Figures 15 and 16 contain all trajectories that score the screen. Each trajectory has a θ_g and a corresponding value of $|\mu|$ as defined in equation (9). The $|\mu|$ for the solid angle and source is determined from the average of the four θ_g 's. The source ΔS is assumed to correspond to the angular flux at θ_0 moving in the direction \underline{e} from the area ΔA as illustrated in Figure 17. The ΔA is thus the area associated with this source for which it is assumed that the angular flux produced about the point dipole by this source is representative over all points of the area ΔA .

$$\Delta A = r_0^2 \sin \theta_0 \Delta \theta_0 \Delta \phi_0 \quad (31)$$

where $\Delta \theta_0$ and $\Delta \phi_0$ define the size of ΔA .

Before proceeding to determine the angular flux distribution about the point dipole, it is essential to compute v_y and Q_1 and compare their values for each trajectory. We have selected a representative set of trajectories that will be used throughout this report to compute various parameters and the angular flux distribution about the point dipole. In Table 2 are given the data corresponding to $\theta = 90^\circ$. These trajectories are enclosed in the rectangular areas outlined by either dotted or solid lines in Figure 14. It can be observed that we have selected certain portions of the total available solid angle region wherein trajectories intersect the screen to cover a wide range range of (ϕ_g, θ_g) points. In all cases, there is reasonable agreement between the values of Q_1 and v_y . We have selected $\theta = 45^\circ$ data for which the selected trajectories are outlined similarly in Figure 15 and these data are given in Table 3. In this case not all of the trajectories give good agreement between Q_1 and v_y . This might be expected where small errors in data produce large errors in $\cos \alpha$, as is the case when \bar{v} is very small in magnitude. Also trajectories that come close to the chamber walls, where the nondipole behavior of the magnet exists, would probably cause discrepancies. This is discussed further in the conclusion section.

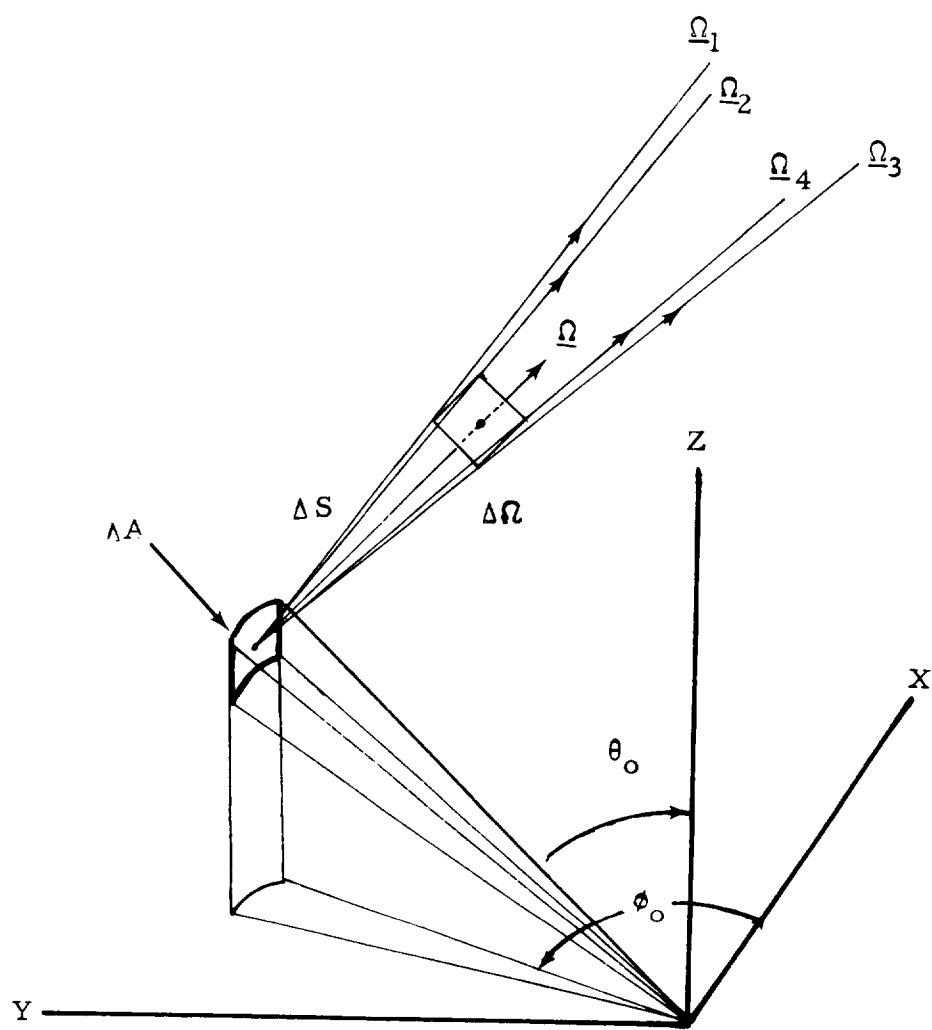


Figure 17. Source angular flux from area, dA .

TABLE 2. TRAJECTORY DATA CORRESPONDING TO $\theta = 90^\circ$

L	ϕ_g	θ_g	\bar{v}	$\cos \alpha_1$	v_y	α_1	α_2	ρ_1	θ_1
965	75.8	93.1	-2.379E-01	-0.5143	-0.4547	121.0	117.0	0.911	-151.4
966	75.8	91.8	-1.996E-01	-0.6142	-0.6565	127.9	131.0	0.939	-156.5
967	77.8	91.8	-1.996E-01	-0.7635	-0.7613	139.8	139.6	0.884	-158.5
968	77.8	93.1	-2.379E-01	-0.6504	-0.6147	130.6	127.9	0.842	-153.7
970	79.7	91.8	-1.996E-01	-0.7867	-0.8966	141.9	153.7	0.861	-158.7
972	79.9	93.2	-2.412E-01	-0.9352	-0.8557	159.3	148.8	0.815	-157.1
975	81.5	93.2	-2.412E-01	-0.9485	-0.5728	161.5	124.9	0.824	-157.3
976	83.5	93.2	-2.412E-01	-0.7823	-0.4091	141.5	114.1	0.916	-155.6
981	81.5	91.8	-1.988E-01	-0.8238	-0.7433	145.5	138.0	0.930	-159.6
982	83.4	91.8	-1.988E-01	-0.6955	-0.7559	134.1	139.1	1.220	-159.5
983	85.4	93.2	-2.412E-01	-0.6446	-0.3222	130.1	108.8	1.164	-154.5
990	96.8	91.8	-1.988E-01	-0.5415	-0.9118	122.8	155.8	1.155	-24.0
991	96.8	93.2	-2.403E-01	0.2289	0.1518	76.8	81.3	1.261	-79.0
992	98.4	93.2	-2.403E-01	0.2080	0.1932	78.0	78.9	1.280	-76.6
993	98.4	91.8	-1.988E-01	-0.6755	-1.0000	132.5	180.0	0.953	-22.4
995	100.4	93.2	-2.403E-01	0.2008	0.1624	78.4	80.7	1.252	-71.6
996	102.3	93.2	-2.403E-01	0.1943	0.1611	78.8	80.7	1.187	-64.8
997	102.3	91.8	-1.988E-01	-0.2588	-0.8300	105.0	146.1	0.861	-29.8
1020	86.8	94.2	-2.724E-01	0.2446	0.1820	75.8	79.5	1.178	-98.6
1021	88.8	94.2	-2.724E-01	0.2628	0.2368	74.8	76.3	1.169	-94.0
1022	88.8	96.1	-3.283E-01	0.4341	0.3551	64.3	69.2	0.934	-95.5
1025	90.7	96.1	-3.283E-01	0.5097	0.4147	59.4	65.5	0.898	-90.0
1026	90.7	94.2	-2.724E-01	0.2697	0.2283	74.4	76.8	1.164	-90.5
1028	92.7	96.1	-3.283E-01	0.5006	0.3489	60.0	69.6	0.898	-84.5
1035	94.6	94.2	-2.724E-01	0.3481	0.2408	69.6	76.1	1.072	-82.0
1066	90.0	100.2	-4.525E-01	0.8764	0.8910	28.8	27.0	0.667	-94.8
1069	91.7	100.2	-4.525E-01	0.8753	0.8801	28.9	28.3	0.667	-85.0
1087	88.8	102.8	-5.276E-01	0.9268	0.8987	22.1	26.0	0.608	-81.8
1088	88.8	104.1	-5.688E-01	0.4081	0.6962	65.9	45.9	0.621	-112.6
1091	90.5	104.1	-5.688E-01	0.7275	0.6093	43.3	52.5	0.626	-86.7
1092	90.5	102.8	-5.276E-01	0.9389	0.9568	20.1	16.9	0.612	-87.0

TABLE 3. TRAJECTORY DATA CORRESPONDING TO $\theta = 45^\circ$

L	ϕ_g	θ_g	$\bar{\gamma}$	Cos α_1	v_y	α_1	α_2	A	θ_1
1441	95.5	87.3	-1.318E-02	0.0521	0.4373	87.0	64.1	0.879	-10.0
1442	95.5	88.6	-4.197E-02	0.0856	-0.3169	85.1	108.5	1.026	-20.0
1549	77.4	94.9	-1.760E-01	0.3261	0.2108	71.0	77.8	1.238	-72.9
1550	77.4	96.0	-2.006E-01	0.4338	0.3501	64.3	69.5	1.109	-80.2
1555	79.4	94.9	-1.760E-01	0.3581	0.2131	69.0	77.7	1.183	-70.5
1556	79.4	96.0	-2.006E-01	0.5174	0.3657	58.8	68.6	1.036	-78.3
1562	81.3	94.9	-1.760E-01	0.4041	0.3021	66.2	72.4	1.118	-68.3
1563	81.3	96.0	-2.006E-01	0.6075	0.4350	52.6	64.2	0.967	-75.5
1570	83.3	94.9	-1.760E-01	0.4739	0.3362	61.7	70.4	1.040	-66.0
1571	83.3	96.0	-2.006E-01	0.7106	0.4427	44.7	63.7	0.898	-72.0
1551	77.4	97.2	-2.253E-01	0.5440	0.3898	57.0	67.1	1.003	-88.8
1557	79.4	97.2	-2.253E-01	0.6133	0.4762	52.2	61.6	0.957	-84.5
1564	81.3	97.2	-2.253E-01	0.6734	0.4501	47.7	63.2	0.916	-79.8
1572	83.3	97.2	-2.253E-01	0.7289	0.5112	43.2	59.3	0.874	-74.9
1582	85.3	97.2	-2.253E-01	0.7904	0.6054	37.8	52.7	0.828	-70.0
1592	85.3	94.7	-1.722E-01	0.4799	0.2315	61.3	76.6	0.990	-59.8
1593	85.3	95.8	-1.951E-01	0.7464	0.4241	41.7	64.9	0.847	-64.4
1605	86.9	94.7	-1.722E-01	0.5044	0.2402	59.7	76.1	0.939	-56.4
1606	86.9	95.8	-1.951E-01	0.7270	0.3907	43.4	67.0	0.824	-59.9
1616	88.9	94.7	-1.722E-01	0.5968	0.3442	53.4	69.9	0.838	-51.8
1607	86.9	97.0	-2.215E-01	0.9052	0.5592	25.2	56.0	0.755	-63.0
1617	88.9	95.9	-1.974E-01	1.0000	0.4933	-0.	60.4	0.690	-54.5
1618	88.9	97.0	-2.215E-01	1.0000	0.6708	-0.	47.9	0.658	-57.1
1675	92.8	86.5	3.967E-03	0.4363	0.9757	64.1	12.6	0.709	1.7
1696	92.8	86.5	3.967E-03	0.8294	0.9747	34.0	12.9	0.709	0.8
1676	92.8	87.8	-2.481E-02	-0.6584	-1.0000	131.2	179.6	0.635	-5.1
1697	92.8	87.8	-2.481E-02	-0.6836	-1.0000	133.1	180.0	0.631	-5.0
1658	94.7	86.5	3.967E-03	0.6999	-0.9625	45.6	164.3	0.686	-1.0
1703	94.8	86.5	3.967E-03	0.7049	-0.9944	45.2	173.9	0.681	-1.0
1657	94.7	87.8	-2.481E-02	-0.6973	-0.8418	134.2	147.3	0.612	-5.0
1704	94.8	87.8	-2.481E-02	-0.4948	-0.8321	119.7	146.3	0.617	-6.0

Some trajectories pass through the screen more than once and the data for the second screen intersection are listed with the trajectory number prefixed with a 9. The data for these are given in Table 4 where most of these trajectories come from $\theta = 90^\circ$ data. Almost all of the data taken with the dipole oriented in the 90° direction gave excellent agreement between Q_1 and v_y values. This is true not only for the above listed trajectories but also when the poles are reversed for which data are presented in Table 5. These include trajectories from 1278 to 1293. A minus prefix is included with several trajectories to study the effect of displacing the measured point to a new (r_1, θ_1) position on the screen. In many cases as the gun is rotated through different small increments of the (ϕ_g, θ_g) angles, the points of the trajectory intersection on the screen trace out a smooth curve (dotted line) as shown in Figure 18. When some of the (r_1, θ_1) points lie off this curve, the point corresponding to a position on the curve is also utilized to compute trajectory data for comparison and this trajectory is designated with a minus prefix. In general, the change produced in Q_1 is very small so that the r_1, θ_1 points could correspond to a point on the smooth curve. Once the data has been shown to give agreement, it is then used to compute the angular flux.

The angular or vector flux $\mathfrak{F}(\underline{r}, \underline{\Omega}) \Delta\Omega$ at \underline{r} is by definition the particle intensity, crossing a unit area perpendicular to $\underline{\Omega}$, having direction $\underline{\Omega}$ and falling within the solid angle $\Delta\Omega$. The four trajectories defining the source ΔS intersect the screen at four separate points (ρ_{1i}, θ_{1i}) each having angular direction α_{1i} . The area, ΔA_s , covered by one solid angle of trajectories is in general one of irregular shape. The area ΔA_s is computed by representing this area as a rectangle whose sides are determined from the averages of (ρ_{1i}, θ_{1i}) .

Thus,

$$\Delta A_s (\bar{z}, \bar{x}) = (\Delta \bar{z}) (\Delta \bar{x}), \quad (32)$$

TABLE 4. TRAJECTORIES WITH MULTIPLE SCREEN INTERSECTIONS

L	ϕ_g	θ_g	$\bar{\gamma}$	Cos α_1	v_y	α_1	α_2	A	θ_1
91019	86.8	96.1	-3.283E-01	-0.5648	-0.6992	124.4	134.4	1.307	-145.8
1019	86.8	96.1	-3.283E-01	0.4115	0.3614	65.7	68.8	0.930	-101.7
1033	94.6	97.4	-3.672E-01	0.5781	0.5535	54.7	56.4	0.801	-77.0
-1033	94.6	97.4	-3.672E-01	0.6230	0.5507	51.5	56.6	0.782	-76.5
91033	94.6	97.4	-3.672E-01	-0.5971	-0.8393	126.7	147.1	0.980	-37.5
1034	94.6	96.0	-3.267E-01	0.5130	0.4216	59.1	65.1	0.879	-79.0
-1034	94.6	96.0	-3.267E-01	0.4939	0.4216	60.4	65.1	0.888	-78.9
91034	94.6	96.0	-3.267E-01	-0.5194	-0.6644	121.3	131.6	1.187	-36.0
1036	96.5	94.2	-2.707E-01	0.3526	0.1858	69.4	79.3	1.054	-77.5
-1036	96.5	94.2	-2.707E-01	0.3243	0.1858	71.1	79.3	1.082	-78.0
91036	96.5	94.2	-2.707E-01	-0.6109	-0.9147	127.7	156.2	0.962	-29.5
1037	96.5	96.0	-3.267E-01	0.4831	0.3695	61.1	68.3	0.865	-72.6
91037	96.5	96.0	-3.267E-01	-0.6061	-0.7999	127.3	143.1	0.769	-33.5
1038	96.5	97.4	-3.688E-01	0.5748	0.5305	54.9	58.0	0.759	-68.8
91038	96.5	97.4	-3.688E-01	-0.5825	-0.4022	125.6	113.7	0.704	-36.2
-91038	96.5	97.4	-3.688E-01	-0.6838	-0.0479	133.1	92.7	0.727	-35.0
1062	88.4	98.8	-4.099E-01	0.7322	0.7767	42.9	39.0	0.718	-101.8
91062	88.4	98.8	-4.099E-01	-0.4321	1.0000	115.6	-0.	1.643	-134.3
1063	88.4	100.2	-4.525E-01	0.7726	0.8425	39.4	32.6	0.672	-103.2
91063	88.4	100.2	-4.525E-01	-0.5527	-0.9991	123.6	177.6	1.335	-134.6

TABLE 5. TRAJECTORIES FOR WHICH THE DIRECTION OF DIPOLE IS REVERSED

L	ϕ_g	θ_g	$\bar{\gamma}$	Cos α_1	v_y	α_1	α_a	ρ_1	θ_1
1278	77.5	92.9	-2.318E-01	0.1972	0.0169	78.6	89.0	1.164	61.7
-1278	77.5	92.9	-2.318E-01	0.1939	0.0169	78.8	89.0	1.169	61.7
91278	77.5	92.9	-2.318E-01	-0.0672	-0.2326	93.9	103.5	0.874	37.7
1279	79.4	92.9	-2.318E-01	0.2166	0.2388	77.5	76.2	1.224	68.9
-1279	79.4	92.9	-2.318E-01	0.1219	0.2388	83.0	76.2	1.243	59.2
91279	79.4	92.9	-2.318E-01	-0.4650	-0.6011	117.7	126.9	0.773	28.4
1280	81.4	92.9	-2.318E-01	0.1990	0.2178	78.5	77.4	1.298	74.0
91280	81.4	92.9	-2.318E-01	-0.8719	-0.0000	150.7	90.0	0.773	23.1
1281	83.0	92.9	-2.318E-01	0.2144	0.1732	77.6	80.0	1.303	78.5
-1281	83.0	92.9	-2.318E-01	0.2089	0.1732	77.9	80.0	1.312	78.5
91281	83.0	92.9	-2.318E-01	-0.7650	-0.9865	139.9	170.6	0.898	24.0
1282	85.0	92.9	-2.318E-01	0.2093	0.2355	77.9	76.4	1.326	81.5
-1282	85.0	92.9	-2.318E-01	0.2066	0.2355	78.1	76.4	1.330	81.5
1288	96.3	92.9	-2.318E-01	-0.6743	-0.4188	132.4	114.8	1.178	156.0
1289	98.3	92.9	-2.318E-01	-0.8396	-1.0000	147.1	180.0	0.976	157.5
-1289	98.3	92.9	-2.318E-01	-0.6973	-1.0000	134.2	180.0	1.349	157.7
1290	100.3	92.9	-2.318E-01	-0.9749	-0.9265	167.1	157.9	0.861	158.5
-1291	101.9	92.9	-2.318E-01	-0.8612	-0.6918	149.4	133.8	0.833	157.0
1292	103.8	92.9	-2.318E-01	-0.7135	-0.6717	135.5	132.2	0.884	155.2
1293	105.8	92.9	-2.318E-01	-0.6993	-0.4602	134.4	117.4	0.971	155.3

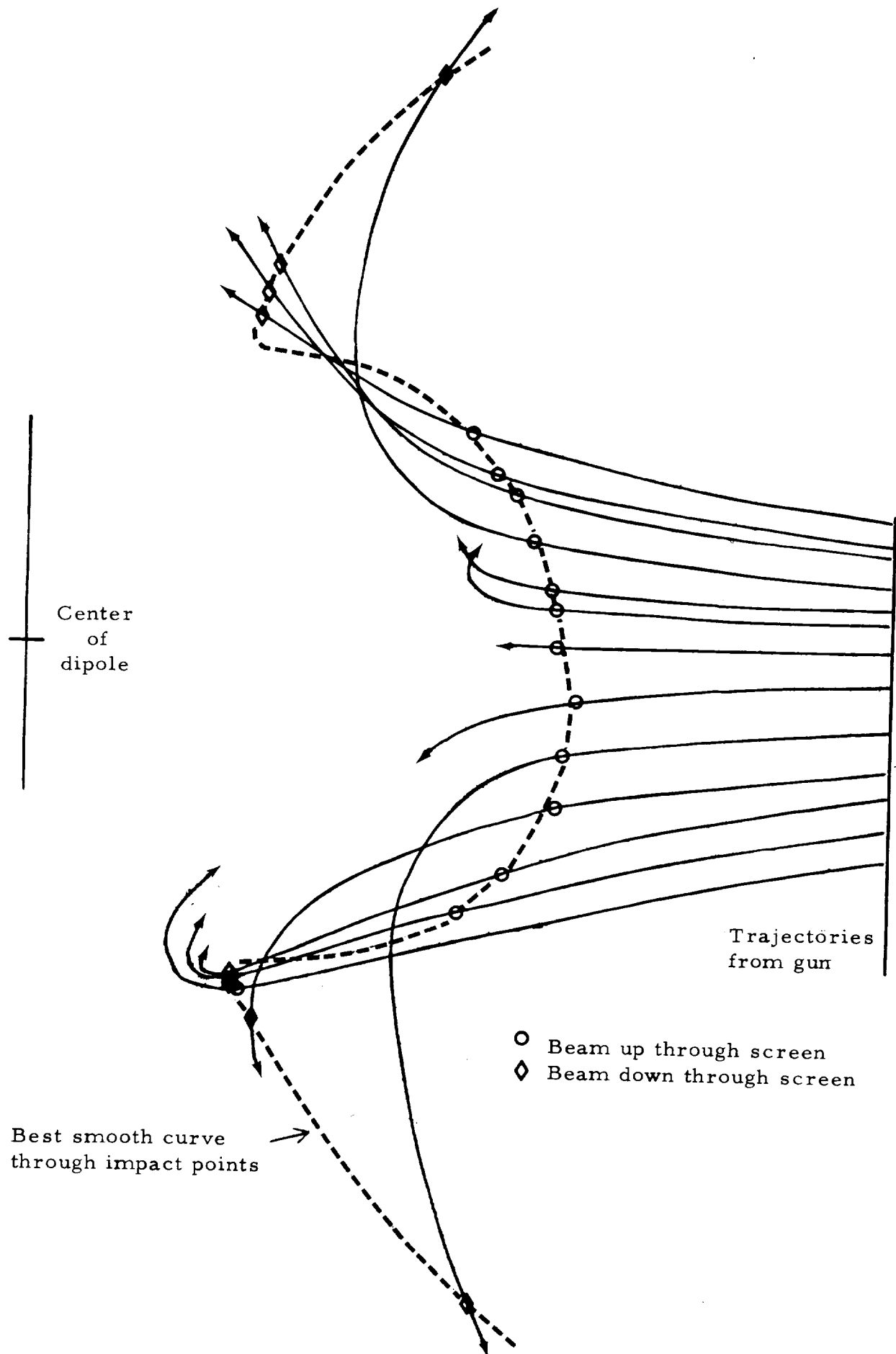


Figure 18. Points of trajectory intersection with screen.

where

$$\bar{z} = \frac{\sum_{i=1}^4 \rho_i \cos \theta_i}{4} \quad \text{and} \quad \bar{x} = \frac{\sum_{i=1}^4 \rho_i \sin \theta_i}{4} \quad (33)$$

and

$$\Delta \bar{z} = \frac{\sum |z_i - \bar{z}|}{2} \quad \Delta \bar{x} = \frac{\sum |\bar{x}_i - \bar{x}|}{2} . \quad (34)$$

Additionally each trajectory has a direction $\underline{\Omega}_i$ at the screen intersection as shown in Figure 19. These angles must use the XYZ axes and not the X' Y' Z' axes, since the effect of rotating the source is achieved by rotating the axes instead. Thus,

$$\underline{\Omega}_i = \underline{i} \sin \alpha_{1i} \cos \theta_{zxi} + \underline{j} \cos \alpha_{1i} + \underline{k} \sin \alpha_{1i} \sin \theta_{zxi},$$

or

$$\underline{\Omega}_i = \underline{i} v_{xi} + \underline{j} v_{yi} + \underline{k} v_{zi},$$

and

$$\Delta \Omega = \sin \bar{\alpha}_1 \Delta \alpha_1 \Delta \theta_{zx} , \quad (35)$$

where

$$\bar{\alpha}_1 = \frac{\sum_{i=1}^4 \alpha_{1i}}{4}$$

$$\Delta \alpha_1 = \frac{\sum |\alpha_{1i} - \bar{\alpha}_1|}{2} , \quad (36)$$

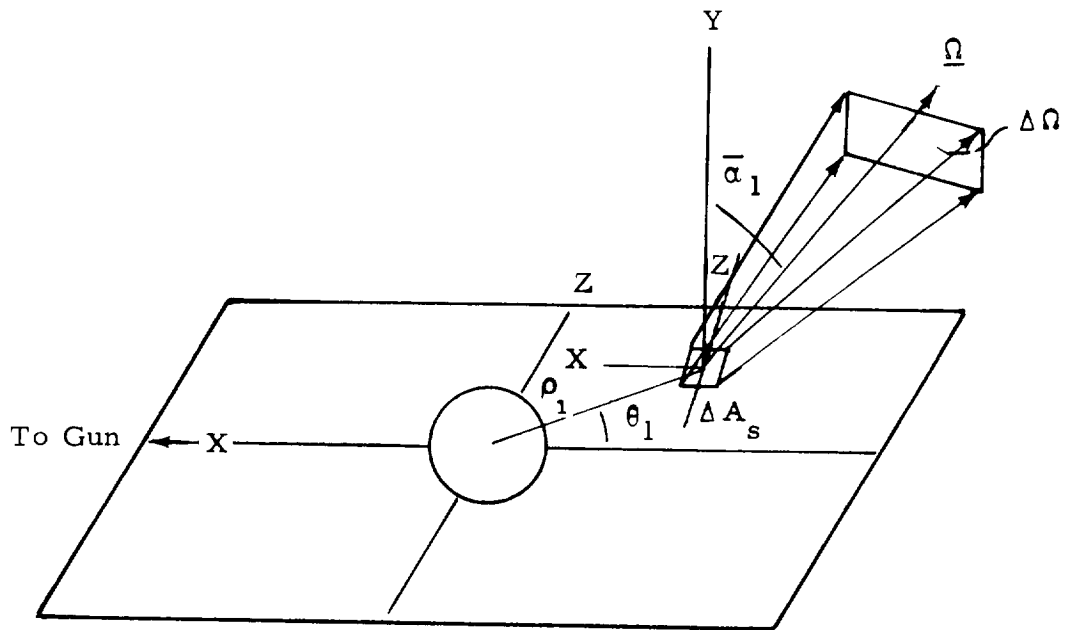


Figure 19. Angular Flux Crossing ΔA_s .

and

$$\Delta \theta_{zx} = \frac{\sum |\theta_{zxi} - \bar{\theta}_{zx}|}{2}.$$

The particle intensity crossing the area ΔA_s having direction $\underline{\Omega}$ and falling within the solid angle $\Delta \Omega$ is ΔS .

The angular flux $\Phi(\underline{r}, \underline{\Omega}) \Delta \Omega$ is thus

$$\Phi(r_1, \underline{\Omega}) \Delta \Omega = \frac{\Delta S}{\Delta A_s \cos \bar{\alpha}_1}. \quad (37)$$

Equation 37 can now be evaluated using eqs. 13, 32, and 35, and this is achieved by the second part of the computer program using the punched cards generated by the first phase of the program.

In evaluating eq. 13, it is necessary to define a ΔA . Theoretically the data should be taken for a large number of θ and ϕ values to obtain a simulated source distribution covering the spherical surface at ρ_0 . Small increments of θ can be obtained by moving the gun over a distance $\rho_0 \Delta \theta_0$, and small increments of ϕ obtained by moving a distance $\rho_0 \sin \theta_0 \Delta \phi$. The increments should be chosen so that the change in angular flux about the point dipole is relatively small. By this procedure the distribution of angular flux is representative of the source at all points on ΔA . In this experiment only two screen positions are used and they are separated by a $\Delta \theta_0 = 45^\circ$. The selection of $\Delta \phi_0 = 45^\circ$ is arbitrary and both $\Delta \theta_0$ and $\Delta \phi_0$ values are too large, and this is discussed further in the conclusion section. It should also be noticed that by changing the gun position from $\theta_0 = 90^\circ$ to $\theta_0 = 45^\circ$, the screen is rotated rather than the gun being repositioned within the tank for obvious reasons. Utilizing screen rotation rather than changing gun position to obtain a complete flux distribution is also discussed in the conclusion.

It is convenient to establish a reference square grid, as shown in Figure 20, for defining areas about the point dipole in which the angular flux can be recorded and summed and the results compared with the calculations of Prescott et al. A grid has been chosen for this task. Each square is 0.025 in Stormer units on a side and there is a total of 100 by 100 squares. Since $C_{st} = 21.73$ cm, each square is 0.543 cm by 0.543 cm and the total area covered by the square is 54.3 cm by 54.3 cm. The screen itself is 61 cm square with the point dipole placed at its center. The dipole has a radius equal to 3 in. or 14.0 squares as shown in Figure 20.

It is the purpose of the program to compute the angular flux crossing these unit squares. Consequently each square is assigned a number (M,N) where

$$M = \frac{\bar{X}}{0.025} + 51 \quad (38)$$

and

$$N = \frac{\bar{Z}}{0.025} + 51 \quad (39)$$

At $\bar{X} = \bar{Z} = -1.25$, $M = N = 1$, defining the first square. Each computation involves the four trajectories of the solid angle $\Delta\Omega_g$ or $\Delta\Omega$, for which \bar{X} and \bar{Z} are determined using eq. 33. The sign of \bar{X} or \bar{Z} is determined by giving θ_1 plus and minus values so as to conform with eqs. 38 and 39 as shown in Figure 20. That is, θ is minus on the side toward the gun.

The angular flux computed by eq. 37 covers one or more squares either completely or partially. The contribution of the flux to any square is at most the value of the flux, $\Phi_{M,N}(\bar{X}, \bar{Z}, \bar{\Omega}) \Delta\Omega$, by definition, and this occurs only when the square is completely contained within ΔA_g . When the flux covers only a fraction, f , of the square, contribution to this square, then the flux $\Phi_{M,N} \Delta\Omega$, is

$$\Phi_{MN} \Delta\Omega = f \cdot \Phi(\bar{X}, \bar{Z}, \bar{\Omega}) \Delta\Omega \quad (40)$$

Equation 40 is evaluated by the second phase of the computer program using punched cards from the first phase as input data. The punched data are the trajectory number, gun angles, ρ_1 , θ_1 , $\cos \alpha_1$, $\theta_z' y'$, and θ_{zx} . With each source radiation solid angle, $\Delta \Omega_g$, there is a corresponding area, ΔA_s , which the radiation covers on the screen as shown schematically in Figure 19. The second phase of the computer program determines the angular flux for each solid angle $\Delta \Omega_g$, the squares contained within ΔA_s , the fraction of area covered for each MN square, and evaluates equation (40) for $\Phi_{MN}(r_1 \Omega) d\Omega$. The data utilize a sequence of connected solid angles so that after the first four trajectories are determined, only two additional trajectories are needed to form each succeeding solid angle, $\Delta \Omega_g$. This continues until further motion of the gun in this region of the $\theta_g \phi_g$ plane no longer involve trajectories that score the screen ending the sequence of connected solid angles. Then another set of such data must be considered. After each set of trajectories, which involve a connected sequence of solid angles, has been evaluated, the computer program prints out a convenient format, (1) the $\Phi_{MN}(\underline{r}, \Omega) d\Omega$ corresponding to each solid angle $\Delta \Omega_g$ in one table, (2) the $\Phi_{MN}(\underline{r}, \Omega) d\Omega$ summed over each set of data in another listing, and (3) the values of the average gun angle ($\bar{\theta}_g$ and $\bar{\phi}_g$), ΔS , \bar{X} , \bar{Z} , $\Delta \bar{X}$, $\Delta \bar{Z}$, $\bar{\alpha}_1$, θ_{zx} , $\Delta \Omega_g$, $\Phi(\underline{r}, \Omega) \Delta \Omega$, EM, EN, $\Delta \Omega$, and the trajectory number associated with each solid angle $\Delta \Omega$ in the third table. Here EM and EN are the fractioned values of \bar{X} and \bar{Z} as determined by eqs. 38 and 39 respectively. The trajectory number printed out is the first of each pair of trajectories. There is an L number for the first four and an additional one for every succeeding two trajectories until the end of the sequence.

Calculation of the angular flux is the last phase of the analysis of the MAGSIM data. This last phase continued to utilize the selected trajectories previously presented in this report but now restricted to those enclosed within the solid lines as outlined in Figures 14 and 15. It can be observed that these data comprise two large and one small solid angle of radiation for the $\theta = 45^\circ$ case. The radiation corresponding to these solid angles illuminates defined areas on the screen as

depicted graphically in Figure 20. The areas, ΔA_s , outlined in Figure 20 are those determined by the second phase of the computer program. The trajectories corresponding to each ΔA_s are also listed within or adjacent to its area in Figure 20. The cross-hatched areas refer to the $\theta = 90^\circ$ configuration. The parameters computed for these trajectories in this phase of the analysis are listed in Table 6 where each connected sequence of solid angles is separated by a space from the others. We have listed in this table the average gun angles $\bar{\theta}_g$ and $\bar{\phi}_g$ used to define the direction $\underline{\Omega}_g$ and necessary in determining $\Delta \Omega_g$. It is easy to reference these sets of trajectories in Figures 14 and 15. The source, ΔS , is essentially the same for all solid angles since this is a result of the experimental procedure. It can be noticed that all of the \bar{X} 's are on the side of the screen toward the gun where the meridian plane vector is up out of the paper. Thus if $\bar{\alpha}_1$ is less than 90° , the trajectories are moving upward through the screen, otherwise they are moving down through the screen. The two areas above and below the dipole are moving down through the screen whereas the region to the left of Figure 20 are moving upwards. The magnitude of $\bar{\Delta X}$ and $\bar{\Delta Z}$ give the sides of ΔA_s in Stormer units and 0.025 is equivalent to one square of the grid. In one case $L = 972$, the $\Delta X = 0.006$ which is a very small region producing a high concentration of flux in that region. The flux appears to be focused at the screen, but this is not necessarily the case. The quantitative value of ΔS proportional to $\underline{\Delta A}$ for which it is assumed that all of the flux in direction $\underline{\Omega}_g$ and in $\Delta \Omega_g$ on this area intersect at ΔA_s . This is clearly not the case here. To obtain a more precise correlation requires integrating the flux passing through ΔA_s when the gun is moved through both small values of $\Delta \theta_0$ and $\Delta \phi_0$ to define ΔA correctly.

It is interesting to compare the relative magnitudes of $\Phi \Delta \Omega$ listed in Table 6. Some directions of the gun will place orders of magnitude greater radiation on the screen even with a small change in solid angle as denoted by L's 972 and 981. In general, one should expect that the beam will become highly divergent at the screen for

TABLE 6 FLUX PARAMETERS FROM PART II OF COMPUTER PROGRAM

L	$\bar{\theta}_g$	ϕ_g	Δs	\bar{x}	\bar{z}	$\Delta \bar{x}$	$\Delta \bar{z}$	$\bar{\alpha}_1$	$\Phi \Delta \Omega$	EM	EN
965	92.4	76.8	4.69×10^{-4}	-0.377	-0.810	0.059	0.064	128.9	0.1959	35.9	18.6
967	92.5	78.8	4.87×10^{-4}	-0.332	-0.783	0.041	0.060	142.5	0.24954	37.7	19.7
972	92.5	80.6	4.29×10^{-4}	-0.318	-0.796	0.006	0.081	141.3	1.09587	38.3	19.2
981	92.5	82.5	4.92×10^{-4}	-0.362	-0.902	0.082	0.241	129.0	0.03978	36.5	14.9
1020	95.1	87.8	6.81×10^{-4}	-1.043	-0.134	0.245	0.097	73.4	0.1007	9.3	45.6
1021	95.1	89.7	6.47×10^{-4}	-1.039	-0.045	0.251	0.080	71.9	0.1003	9.4	49.2
1087	103.4	89.6	3.78×10^{-4}	-0.603	-0.021	0.031	0.218	35.3	0.0697	26.9	50.2
1555	95.4	80.3	2.65×10^{-4}	-1.026	0.315	0.102	0.178	70.7	0.0443	10.0	63.6
1562	95.4	82.3	2.79×10^{-4}	-0.945	0.339	0.099	0.158	67.7	0.0466	13.2	64.6
1570	95.3	84.3	2.79×10^{-4}	-0.856	0.391	0.094	0.139	68.9	0.0592	16.8	66.6
1556	96.6	80.3	2.88×10^{-4}	-0.951	0.177	0.065	0.099	64.4	0.1038	13.0	58.1
1563	96.6	82.3	3.03×10^{-4}	-0.884	0.227	0.070	0.065	62.6	0.1443	15.6	60.1
1571	96.5	84.3	3.28×10^{-4}	-0.810	0.289	0.078	0.077	60.1	0.1092	18.6	62.5
1696	87.1	93.7	3.15×10^{-4}	-0.028	0.659	0.054	0.076	126.0	0.1302	49.9	77.4

those gun angles which fall on the periphery of the enclosed regions of Figures 15 and 16. In the last two columns, EM and EN, the \bar{x} and \bar{z} positions are given in fractional values of M and N which are reserved for the whole numbers used to identify the location of the unit areas in the grid of Figure 20.

The flux $\Phi(r)$ as defined by Prescott et al is proportional to $\Phi_{MN} \Delta\Omega$. A direct comparison between theory and experiment requires integrating the experimental data over a small ΔA as explained earlier. Once this is accomplished, the procedure in this report gives $\Phi(r)/\Phi(\infty)$ directly. That is,

$$\sum \Phi_{MN} \Delta\Omega = \Phi(r)/\Phi(\infty).$$

However, the theoretical calculation assumes an infinitesimal point dipole that does not interfere with the trajectories. Thus the experiment could provide a measure of the shadow effect produced by the 6-in. - diameter point dipole.

The curves depicting $\Phi(r)/\Phi(\infty) = 0$ and $= 1$ from Prescott et al are given in Figure 20. The intensities of the flux $\Phi_{MN} \Delta\Omega$ have been computed for the data shown in Figure 20 where the values are summed over all of the trajectory data employed in the analysis. Even these areas cover such a large number of MN areas that it is not convenient to list them all in this report. Consequently only a partial listing of these data are given in Table 7; however, the data are selected to be representative of the total ensemble. In general, the flux intensity produced when the dipole is oriented at $\theta = 90^\circ$ produces more intense radiation at the screen than does that from the $\theta = 45^\circ$ configuration.

TABLE 7. LISTING OF $\Phi_{MN} \Delta \Omega$

(M, N)	$\Phi_{MN} \Delta \Omega$	(M, N)	$\Phi_{MN} \Delta \Omega$	(M, N)	$\Phi_{MN} \Delta \Omega$
1, 41	0. 2333E-01	9, 58	0. 7192E-01	3, 49	0.1552E-00
1, 42	0.1007E-00	10, 55	0. 6589E-01	3, 50	0.1033E-00
1, 43	0.1007E-00	10, 56	0. 8879E-01	3, 51	0.1033E-00
1, 44	0.1007E-00	10, 57	0.1102E-00	3, 52	0. 4195E-01
1, 45	0.1038E-00	10, 58	0.1463E-00	4, 41	0. 2333E-01
1, 46	0. 2040E-00	11, 69	0. 9096E-01	4, 42	0.1007E-00
1, 47	0. 2040E-00	11, 70	0. 7393E-01	4, 43	0.1007E-00
2, 48	0. 2040E-00	12, 54	0. 9383E-01	4, 44	0.1007E-00
2, 49	0.1552E-00	12, 55	0.1037E-00	4, 45	0.1038E-00
2, 50	0.1033E-00	12, 56	0.1266E-00	4, 46	0. 2040E-00
2, 51	0.1033E-00	14, 68	0.1067E-00	6, 44	0.1007E-00
2, 52	0. 4195E-01	14, 69	0.1067E-00	6, 45	0.1038E-00
3, 41	0. 2333E-01	14, 70	0.1016E-00	6, 46	0. 2040E-00
3, 42	0.1007E-00	14, 71	0. 5924E-01	6, 47	0. 2040E-00
3, 43	0.1007E-00	14, 72	0.1156E-01	6, 48	0. 2040E-00
7, 70	0. 3218E-01	20, 65	0.1012E-00	6, 49	0.1552E-00
8, 56	0. 2289E-01	20, 66	0. 3146E-01	6, 50	0.1033E-00
8, 57	0. 4432E-01	20, 67	0. 3146E-01	6, 51	0.1033E-00
8, 58	0. 4432E-01	20, 68	0. 3146E-01	6, 52	0. 4195E-01
8, 59	0. 4432E-01	20, 69	0. 3146E-01	7, 41	0. 2333E-01
8, 60	0. 4432E-01	20, 70	0. 3146E-01	7, 42	0.1007E-01
8, 61	0. 4432E-01	51, 77	0.1302E-00	7, 43	0.1007E-00
8, 67	0. 4432E-01	51, 78	0.1302E-00	7, 44	0.1007E-00
8, 68	0. 4432E-01	51, 79	0.1302E-00	7, 45	0.1038E-00
8, 69	0. 4432E-01	51, 80	0. 5511E-01	7, 46	0. 2040E-00
8, 70	0. 3218E-01	52, 74	0. 3176E-02	8, 51	0.1033E-00
9, 56	0. 2289E-01	52, 75	0. 4646E-02	8, 52	0. 4195E-01
9, 57	0. 4432E-01	3, 48	0. 2040E-00	9, 41	0. 2333E-01

CONCLUSIONS

The MAGSIM has now been modified to measure with useful accuracy trajectory parameters associated with the motion of a charged particle in a magnetic field. Although a technique has been effected for experimentally determining the angular or vector flux distribution about the point dipole, the system can be used to obtain other interesting trajectory information. The patterns displayed in Figures 12 and 13, showing the angular directions of the gun for which trajectories score the screen, can be useful in several ways. First the earth is a near point dipole magnet so that work performed on this contract is relevant to high energy charged particles penetrating the earth's magnetic field. It may be desirable to study incident directions of charged particles in real space that come close to the earth. The region about the earth can be defined by the screen and the screen does not need to be square, it can take on any shape desired; a circle, annular ring, etc., to define the region of interest near the earth or magnet. In this regard, certain annular regions about the earth might be important for future manned earth orbiting stations. Thus studies of this type relate allowed directions for charged particle intersecting the screen to defined regions in space. Such data can also be used in support of trajectory calculations in that they define those trajectories which pass close to the earth or magnet and eliminates the need for performing any calculations to determine the important or relevant trajectories.

When more quantitative data are desired, Figures 15 and 16 can be very useful. In these sets of figures the gun's angular direction for a particular point in space is directly related to the vector flux and the solid angle $\Delta\Omega$ at the screen. It should be repeated, however, that the quantitative value of the vector flux $\Phi_{MN} \Delta\Omega$ is proportional to ΔA . The values reported in Table 7 are based on $\Delta\phi_0 = \Delta\theta_0 = 45^\circ$. Reducing these to increments 1° will reduce the magnitude of the flux by $\left(\frac{1}{45}\right)^2$. Consequently, it will be necessary to take such data for several $(\rho_0, \theta_0, \phi_0)$ positions of the gun about the area so that an integration can be

made over a small area ΔA . This will require moving the gun in increments sufficiently small to produce a reasonable change in the angular flux distribution about the point dipole. For each position $(\rho_0, \theta_0, \phi_0)$ of the gun, a flux distribution is produced in the MN plane of Figure 19. By systematically taking data in the required increments to cover the full spherical surface at ρ_0 , a pattern of the flux intensity, $\Phi_{MN} \Delta \Omega$, will be generated in the MN plane that can be compared with results predicted by Prescott et al. In this case, however, the shadow effect of the magnet will cause the $\Phi_{MN}(r, \Omega) \Delta \Omega$ pattern to be different. In fact, such data can be used to study the shadow effect directly. It is not necessary to take data covering all source positions on the surface for a cylindrically symmetric magnet like the point dipole. Data taken in one quadrant can be used to derive the data corresponding to symmetrical positions in the other three quadrants when integrating over the ϕ direction; however, changes in θ must be made to cover the full 2π range.

From the limited data obtained in this experiment, there exists a very large variation in flux divergence at a point on the screen, depending on where the trajectory originates from in space and its initial direction. In some cases a particular gun direction will produce a relatively concentrated beam at the screen. In view of the constraint $\Phi(r)/\phi(\infty) \leq 1$, it is believed that the sources of flux at a particular point near the screen come principally from a few selected points and directions in space. The remaining flux comes from numerous points in space that produce a highly diffuse beam to cover the area. This would be in agreement with other work⁷ performed on the MAGSIM where it was observed that the cylindrically symmetric flux exhibiting a 60° loss cone (Van Allen Belt radiation) produces a forbidden volume at the center of a circular loop magnet.

For the experimental setup used here, movement of the gun about the dipole is highly limited. It is far more convenient to rotate the screen to achieve the same effect; however, because of the fixed camera position, the data reduction is made more complex. Nevertheless, it is possible to achieve a reasonable coverage by this

manner. First, the screen should be rotated about the Y axis of Figure 19 to simulate moving the source through θ similar to that performed in this study. Once a quadrant is covered, then it would be necessary to tilt the screen so that the Y axis now makes an angle ϕ with the former axis Y' . By rotating the screen about the $\underline{Y'}$ axis, the effect of moving the screen through the angle θ in $\Delta\theta$ increments for the new ϕ position can be simulated. This procedure becomes less accurate the larger ϕ , if the two cameras remain fixed as they must in the present system. By this means, a complete simulation of flux in space can in principle be achieved with the present system.

The data obtained in this experiment are self-consistent for the $\theta = 90^\circ$ position for almost all trajectories including those that score the screen more than once. For the $\theta = 45^\circ$ data there were a sufficient number of discrepancies between the directly measured values of $Q_1 = v_y$ and the corresponding values computed based on a constant \bar{y} that a preliminary study of the errors associated with these measurements has been performed. The trajectories chosen for this preliminary error analysis are given in Table 8 together with other pertinent parameters. They are listed in a sequence convenient for this analysis.

Before proceeding with this discussion, it should be remembered that the v_y is determined from the trajectory at the point of the screen, whereas the $\cos \alpha_1$ is computed from the gun angles and ρ_1 and θ_1 . In the latter case, should the trajectory pass through regions where the magnetic field is slightly different from that of a point dipole, it will cross the screen at an angle different from what point dipole theory would predict. The net result will be to produce a difference between the two answers for Q_1 . Such non-dipole behavior can occur at large distances from the point dipole where its field is weak. This particular experiment is quite susceptible to such effects since the vacuum tank's walls are constructed of steel. Such effects will occur prior to the trajectory moving toward the screen and will probably have the effect of simulating the different \bar{y} or θ_g . It is not expected, however, that

TABLE 8. TRAJECTORIES USED FOR ERROR ANALYSIS

L	ϕ_g	θ_g	$\bar{\gamma}$	A	θ_1	Cos α_1	\hat{v}_y	α_1	αa	$\theta_z' y'$	$\theta_z' x'$	$\theta_y' x'$
1441	95.5	87.3	-0.0132	0.879	-10.0	0.0521	0.4373	87.0	64.1	-17.5	171.2	26.2
1442	95.5	88.6	-0.042	1.026	-20.0	0.0856	-0.3169	85.1	108.5	29.7	169.0	-18.8
1658	94.7	86.5	+0.004	0.631	-5.0	0.6999	-0.9625	45.6	164.3	11.7	132.6	-79.2
1703	94.8	86.5	+0.004	0.681	-1.0	0.7049	-0.9944	45.2	173.9	4.5	132.5	-85.9
1657	94.7	87.8	-0.025	0.612	-5.0	-0.6973	-0.8418	134.2	147.3	-24.6	-134.5	-65.8
1704	94.8	87.8	-0.025	0.617	-6.0	-0.4948	-0.8321	119.7	146.3	-27.4	-129.1	-67.2
1675	92.8	86.5	-0.004	0.709	1.7	0.4363	0.9757	64.1	12.6	9.0	45.1	81.0
1696	92.8	86.5	-0.004	0.709	0.8	0.8294	0.9747	34.0	12.9	9.2	45.1	80.8
1676	92.8	87.8	-0.025	0.635	-5.1	-0.6584	-1.000	131.2	179.6	0.3	-41.0	-89.7
1697	92.8	87.8	-0.025	0.631	-5.0	-0.6836	-1.000	133.1	180.0	0.0	-35.0	-90.0
*1605	86.9	94.7	-0.172	0.939	-56.4	0.5044	0.2402	59.7	76.1	-2.8	179.3	13.9
1606	86.9	95.8	-0.195	0.824	-59.9	0.7270	0.3907	43.4	67.0	-1.2	179.5	23.0
1607	86.9	97.0	-0.222	0.755	-36.0	0.9052	0.5592	25.2	56.0	-7.2	175.1	34.1
1616	88.9	94.7	-0.172	0.838	-51.8	0.5968	0.3442	53.4	69.9	-13.1	175.1	20.2
1617	88.9	95.9	-0.197	0.690	-54.5	1.000	0.4933	0	60.4	-16.2	170.5	29.9
1618	8.9	97.0	-0.222	0.658	-57.1	1.000	0.6708	0	47.9	-10.0	170.8	42.5

such trajectories will occur that approach the completely forbidden volume. Past experiments on measuring completely forbidden volumes have provided accurate results.

For the first case, consider trajectories 1441 and 1442. Here the initial discrepancy was traced to an error in the data. As explained in the appendix, the $\theta_{y'x'}$ carries a minus sign if the trajectory is in the opposite direction of the meridian plane vector. The minus sign was accidentally not included for trajectory 1441. Changing the sign of 1441's $\theta_{y'x'}$ gives $v_y = -0.4373$ and $= 115.9^\circ$ which are consistent with corresponding results for 1442, although in the opposite direction of that predicted by $\cos \alpha_1$. The positive X axis is toward the gun so that the meridian plane vector is upwards on this side and downwards on the other side. Consequently the 1440 and 1441 trajectories are observed to be going up through and almost parallel to the screen. The predicted values are also moving nearly parallel to the screen, but in the downward direction, so that the difference between the angles α_1 and α_2 for the two trajectories are not very great.

The trajectories 1441 and 1442 fall into a similar class with the trajectories 1658, 1703, 1657, 1704, 1675, 1696, 1676, and 1697 where the \bar{v} values are very small and are thus sensitive to either real or apparent errors in θ_g . This tends to explain the larger differences exhibited between α_1 and α_2 for these trajectories and indicates that the steel chamber wall is perturbing their motion. It should be noted that the above eight trajectories are in reality only four since half are repeats. The data are consistent within trajectory pairs and provide an estimate of the precision of the measurements. Although the data repeat as shown, the larger differences do occur for the very small values of \bar{v} . Since the α_2 is determined from direct measurements of the velocity vector, it is used in computing the solid angle $\Delta\Omega$ at the screen.

Another effect that can introduce errors in α_2 concerns the construction of \bar{v} from the vector components. When $|\theta_{y'x'}| = 90^\circ$

the trajectory is moving in a near line of sight with the side camera (View 2). Thus, $\tan \theta_{y'x'} \rightarrow \infty$ and introduces large errors. This may partly explain the α_1 and α_2 differences for trajectories 1675 and 1696.

Except for the last two trajectories, the large value of $\bar{\gamma}$ give excellent results between the two methods as can be seen by reviewing all of the data. In these two cases, the Q_1 is very sensitive to ρ_1 or σ_1^2 . Another calculation was made where r_1 was increased by 1 cm (ρ_1 increased by 0.005 Stormer Units). This kind of error can occur in some cases when the electron beam is concentrated so that the major portion passes through the grid with only the edge of the beam striking the wires. The results of this calculation is shown in Table 9, where better agreement occurs for trajectories 1607, 1616, 1617, and 1618, but not necessarily for the others; however, only 1616 and 1617 appear to be very sensitive to an error in ρ_1 .

The techniques evolved through this study can be extremely useful not only in active shield studies for future manned spacecraft, but also for determining charge particle motion in the earth's magnetic field. For future extensive studies on trajectories as performed in this program, it is recommended that a new MAGSIM be constructed, designed specifically for this purpose. The system should incorporate a non magnetic vacuum chamber and have provision for moving the gun about the magnet. Flexibility in camera positions are also required. The method for taking data and performing data analysis can be automated to a higher degree than has been accomplished here. By these means a system could be achieved for obtaining trajectory data of charged particle motion in a magnetic field more expediently and economically than can be attained by any other method. Modified point dipoles could be used to more closely simulate the earth's magnetic field to achieve greater accuracy here. Finally, the system can be used to study the integrity of any active shield and should be especially useful where materials are also to be incorporated into the protective design.

TABLE 9. TRAJECTORY PARAMETERS WHERE R_1 HAS BEEN INCREASED 1 CENTIMETER

L	α_1	α_2	ρ_1	θ_1
*1441	87.8	115.9	0.925	-10.0
1442	86.2	108.1	1.077	-20.0
1658	49.2	164.3	0.732	-1.0
1703	48.8	173.9	0.727	-1.0
1675	131.6	147.3	0.658	-5.0
1704	118.6	146.3	0.663	-6.0
1675	66.0	12.6	0.755	1.7
1696	39.0	12.9	0.755	0.8
1676	128.9	179.6	0.681	-5.1
1697	130.6	180.0	0.677	-5.0
1605	64.0	76.1	0.985	-56.4
1606	51.3	67.0	0.870	-59.9
1607	39.8	56.0	0.801	-63.0
1616	59.3	69.9	0.884	-51.8
1617	32.6	60.4	0.736	-54.5
1618	22.0	47.9	0.709	-57.1

* Corrected (uses $\theta_{y'x'} = -26.6$)

REFERENCES

1. C. Stormer, "The Polar Aurora," Clarendon Press, 1955.
2. R. H. Levy, AVCO-Everett Research Lab. Report 106 (1961).
3. R. F. Tooper, "Electromagnetic Shielding Feasibility Study," Aeronautical Systems Div., ASD-TDR-63-194.
4. A. Bhattacharjie and I. Michael, AIAA j. 2, 2198, 1961.
5. S. H. Levine and R. Lepper, "Analog Studies of Magnetic Shields," AIAA j. Vol. 4, No. 4, April 1968.
6. S. H. Levine and R. Lepper, "Magnetic Shield Simulator," Institute of Environmental Sciences' 1965 Annual Technical Meeting Proceedings.
7. S. H. Levine and R. Lepper, "Analogue Studies of Active Radiation Shielding," Technical Report AFFDL-TR-66, May 1967.
8. A. D. Prescott, E. W. Urban, and R. D. Shelton, "Second Symposium on Protection Against Radiation in Space," held at Gatlinburg, Tennessee, p. 189, 1964.
9. E. W. Urban, J. of Math. Phys., 6, 1966, 1965.
10. K. M. Case, F. de Hoffmann and G. Placzek, "Introduction to the Theory to Neutron Diffusion," Los Alamos Scientific Laboratory, June 1953.
11. K. G. Malmfors, "Determination of Orbits in the Field of a Magnetic Dipole with Applications to the Theory of the Diurnal Variation of Cosmic Radiation," Arkiv for Matematik, Astronomi Och Fysik, Band 32 A. No 8.
12. S. H. Levine, A. Bhattacharjie, and R. Lepper, "Forbidden Regions Produced by Two Parallel Dipoles," presented to AIAA, May 1966.

APPENDIX

A computer program has been written in FORTRAN-4 language to support the data reduction and analysis. The program consists of two parts. The first part is used to compare values of Q_1 determined by two separate methods in assessing the accuracy and consistency of the data, and the second part computes the angular flux and other pertinent trajectory parameters. Although a right-handed coordinate system about the point dipole is employed in the data analysis, there remains some flexibility in relating the data calculated in the first part to that in the second part. This is the case with θ_1 where this angle is measured to be positive on the side of the axis away from the gun along the negative X axis. By such means, the calculation of the M and N grid is consistent with the top view of the grid. It was also necessary to relate the angle between the meridian plane vector and the velocity vector when deriving the velocity vector from the photographed vector components. The nomenclature used here was to prefix θ with a minus sign when the vector is greater than 90° . The programs are presented in precise format, each line representing one IBM card. The definition of symbols used in the computer program and their equivalent in the text are as follows:

L	=	trajectory number
H	=	voltage reading for gun angle corresponding to ϕ_g
V	=	voltage reading for gun angle corresponding to θ_g
PH	=	ϕ_g = gun angle in horizontal plane
A	=	θ_g = gun angle in vertical plane
G	=	$\bar{\gamma}$ = constant of motion
TH1	=	θ_1 = cylindrical coordinate of trajectory in screen grid
RI	=	r_1 = cylindrical coordinate of trajectory in screen grid
AI	=	α_1 = angle trajectory makes with meridian plane vector at screen
TH3	=	$\theta_{z'x'}$ = angle of velocity vector component in axes parallel to camera's view

TH4	=	$\theta_{y'x'}$ = angle of velocity vector component in axes parallel to camera's view
TH5	=	$\theta_{z'y'}$ = angle of velocity vector component in axes parallel to camera's view
TH6	=	θ_{zx} = angle of velocity vector component in axes aligned with dipole axis
V_y	=	$\cos \alpha_2$ = same as $\cos \alpha_1$ except computed from velocity vector components
A_2	=	$\alpha_2 = \cos^{-1} V_y$
AP	=	α^1 = uncorrected gun angle ϕ_g
BP	=	θ^1 = uncorrected gun angle θ_g
G1	=	\bar{y} calculated from V_y
A_3	=	α_0 calculated from G1
P	=	ρ_0 = distance between point dipole and gun in S. U.
P_0	=	ρ_0 calculated from G1
TH6	=	θ_{zx} = velocity vector angle in dipole coordinate axis
P1	=	$\rho_1 = r_1$ is S. U.
TH	=	θ_0 = angle between dipole axis and AA' of Fig
AA	=	Average value of θ_g in $\Delta\Omega_g$
PHA	=	Average value of $\phi_g = \Delta\Omega_g$
DQ	=	ΔS = source intensity from area ΔA
ZA	=	Average value of $\rho \cos \theta_1$
XA	=	Average value of $\rho \sin \theta_1$
DZA	=	ΔZ of area ΔA_s on screen
DXA	=	ΔX of area ΔA_s on screen
A_2A	=	Average value of α_2 in $\Delta\Omega$
TH6A	=	Average value of θ_{zx} in $\Delta\Omega$
OM1	=	$\Delta\Omega$ = solid angle of flux irradiating screen
OM	=	$\Delta\Omega_g$ = solid angle of source radiation ΔS
DTH	=	$\Delta\theta_0$ = angle increment defining ΔA
DPHO	=	$\Delta\phi_0$ = angle increment defining ΔA
CU	=	$\Phi(r, \Omega) \Delta\Omega$ = angular flux
FL	=	$\Phi_{MN} \Delta\Omega$ = angular flux covering the MN square
F	=	fraction of MN area covered by radiation from source ΔS .

PART I - CHARGE PARTICLE MOTION COMPUTER PROGRAM

```

MAG2 - EFN SOURCE STATEMENT - IFN(S)

DIMENSION L(100), H(100), V(100), PH(100), A(100), G(100) TH1(100
1), R1(100), A1(100), TH3(100), TH4(100), TH5(100), VY(100), A2(100
2), CSA1(100), AP(100), BP(100), G1(100), A3(100), P(100), PO(100)
3, TH6(100), P1(100)
1 READ(5,100)N,ID,TH,B0,B1,B2,B3,C0,C1,C2,C3,B4
100 FORMAT(216,10F6.0)
8 READ(5,500)C4,D1,D2,W,R
500 FORMAT(12F6.0)
1 READ(5,200)(L(I),H(I),V(I),R1(I),TH1(I),TH4(I),TH6(I),
1 TH3(I),I=1,N)
200 FORMAT(16,7F6.0)
CST=0.12586*SQRT(W)
P(1)=R/CST
WRITE(6,600) P(1),CST
600 FORMAT(1H110X3HP=F6.3,7X5HCST=F6.2)
WRITE(6,300)
300 FORMAT(1H 4X1HL4X2HPH7X1HA10X1HCG9X4HCSA16X2HVY6X2HA16X2HA26X 3H
LINES=0
DO10 I=1,N
IF(H(I)-B4)2,2,3
2 AP(I)=B0+B1*H(I)
GO TO 4
3 AP(I)=B2+B3*H(I)
4 IF(V(I)-C4)5,5,6
5 BP(I)=C0+C1*V(I)
GO TO 7
6 BP(I)=C2+C3*V(I)
7 PH(I)=AP(I)+D1
A(I)=BP(I)+D2
IF(ID.EQ.0) A(I)=180.0-A(I)
G(I)=.5*P(1)*SIND(TH)*COSD(A(I))-SIND(TH)**2/P(1))
P1(I)=R1(I)/CST
CSA1(I)=(ABS(SIND(TH1(I)))/P1(I)**2)+(2.*G(I)/(P1(I)*ABS(SIND(TH1
1(I))))

```

	MAG2	-	EFN	SOURCE STATEMENT	-	IFN(S)
				IF(CSA1(I).LT.-1.) CSA1(I)=-1.		
				IF(CSA1(I).GT.1.) CSA1(I)=1.		
				A1(I)=ACOSD(CSA1(I))		
				TN=SIND(TH3(I)*COSD(TH4(I))/(COSD(TH3(I))*SIND(TH3(I)*COSD		
				VY(I)=1./SQRT(1.+(COSD(TH4(I))/SIND(TH4(I)))**2+(TN)**2)		
				IF(TH4(I).LT.0.) VY(I)=-VY(I)		
				TH5(I)=ATAND(TN)		
				A2(I)=ACOSD(VY(I))		
				G1(I)=(ABS(SIND(TH1(I)))/2.)*(P1(I)*COSD(A2(I))-ABS(SIND(TH1(I)))/		
				P1(I))		
				CSA3=(SIND(TH)/P(1)**2)+2.*G1(I)/P(1)*SIND(TH)		
				A3(I)=ACOSD(CSA3)		
				BB=G1(I)/COSD(A(I))*SIND(TH)		
				X=BB**2+SIND(TH)/COSD(A(I))		
				IF(X.LT.0.0) X=0.		
				PO(I)=BB+SQRT(X)		
900				WRITE(7,900)L(I),A(I),PH(I),P1(I),TH1(I),A2(I),TH5(I),A1(I),TH6(I)		
				FORMAT(I6,2F6.1,F6.3,5F6.1)		
				LINES=LINES+1		
				IF(LINES.GT.40)GO TO 20		
				GO TO 10		
20				WRITE (6,700)		
700				FORMAT(1H1)		
				LINES=1		
				WRITE (6,300)		
10				WRITE (6,400)L(I),PH(I),A(I),G(I),CSA1(I),VY(I),A1(I),A2(I),TH5(I),		
				1TH3(I),TH4(I),P1(I),TH1(I),A3(I),P0(I)		
400				FORMAT(IH I6,2F8.1,1PE14.3,OP2F9.4,5F8.1,1F8.3,F6.1,F8.1,F9.3)		
				GO TO 1		
				END		

PART II - CHARGE PARTICLE MOTION COMPUTER PROGRAM

```

MAG3      -   EFN      SOURCE STATEMENT      -   IFN(S)      -

DIMENSION Z(100), X(100), A(100), PH(100), P1(100), TH1(100), A2(100), TH
16(100), FL(100,100), AA(100), PHA(100), DQ(100), ZA(100), XA(100), DZA(10
20), DXA(100), A2A(100), TH6A(100), OM1(100), DZ(100), DX(100), A1(100), OM
3(100), CU(100), EM(100), EN(100), TH5(100), L(100)
1      READ(5,100) TH,DTH,DPHO,P,XL1,XL2,N
100     FORMAT(6F6.0,I6)

200     READ(5,200)(L(I),A(I),PH(I),P1(I),TH1(I),A2(I),TH5(I),A1(I),TH6(I)
      1,I=1,N)

      FORMAT(I6,8F6.0)
      WRITE(6,500)XL1,XL2
500     FORMAT(1H10X3HL1=F6.0,7X3HL2=F6.0)
      DAR=(P**2)*SIND(TH)*DPHO*DTH*0.01745*0.01745
      DO 11 I=1,N
          Z(I)=P1(I)*COSD(TH(I))
          X(I)=P1(I)*SIND(TH(I))
          IMAX=N-2
          DO10 I=1,IMAX,2
              PHA(I)=(PH(I)+PH(I+1)+PH(I+2)+PH(I+3))/4.0
              AA(I)=(A(I)+A(I+1)+A(I+2)+A(I+3))/4.0
              DA=(ABS(A(I)-AA(I))+ABS(A(I+1)-AA(I))+ABS(A(I+2)-AA(I))+ABS(A(I+3)
              1-AA(I)))/2.0
              DPH=(ABS(PH(I)-PHA(I))+ABS(PH(I+1)-PHA(I))+ABS(PH(I+2)-PHA(I))+ABS
              1(PH(I+3)-PHA(I)))/2.0
              OM(I)=SIND(AA(I))*DA*DPH*(0.01745)**2
              DQ(I)=(ABS(COSD(AA(I)+90.0))*OM(I)*DAR)/12.566
              ZA(I)=(Z(I)+Z(I+1)+Z(I+2)+Z(I+3))/4.0
              XA(I)=(X(I)+X(I+1)+X(I+2)+X(I+3))/4.0
              EM(I)=(XA(I)/0.025)+51.0
              EN(I)=(ZA(I)/0.025)+51.0
              DZA(I)=(ABS(Z(I)-ZA(I))+ABS(Z(I+1)-ZA(I))+ABS(Z(I+2)-ZA(I))+ABS(Z(
              1I+3)-ZA(I)))/2.0
              DXA(I)=(ABS(X(I)-XA(I))+ABS(I+1)-XA(I))+ABS(X(I+2)-XA(I))+ABS(X(

```

MAG3	-	EFN	SOURCE STATEMENT	-	IFN(S)
1I+3)-XA(I))/2.0					
DARS=DZA(I)*DXA(I)					
CUR=DQ(I)/DARS					
A2A(I)=(A2(I)+A2(I+1)+A2(I+2)+A2(I+3))/4.0					
TH6A(I)=(TH6(I)+TH6(I+1)+TH6(I+2)+TH6(I+3))/4.0					
DTH6=(ABS(TH6(I)-TH6A(I)+ABS(TH6(I+1)-TH6A(I)+ABS(TH6(I+2)-TH6A(I)+ABS(PH1(I+3)-PH(I))/2.0					
DA2=(ABS(A2(I)-A2A(I))+ABS(A2(A2(I+1)-A2A(I))+ABS(A2(I+2)-A2A(I))+ABS(1(A2(I+3)-A2A(I))/2.0					
OM1(I)=(SIND(A2A(I)))*DA2*DPH1*(0.01745)**2					
CU(I)=CUR/ABS(COSD(A2A(I)))					
Z1=ZA(I)-DZA(I)					
Z2=Za(I)+DZA(I)					
X1=XA(I)-DXA(I)					
X2=XA(I)+DXA(I)					
M1=(X1/0.025)+51.0					
M2=(X2/0.025)+51.0					
N1=(Z1/0.025)+51.0					
N2=(Z2/0.025)+51.0					
EM1=M1					
EM2=M2					
EN1=N1					
EN2=N2					
DO20 M=M1, M2					
DO20 N=N1, N2					
IF(M.EQ.M1,ORM.EQ,M2,OR,N.EQ.N1,OR,N.EQ.N2)GO TO 21					
FL(M,N)=FL(M,N)+CU(I)					
GO TO 20					
DELZ=1.0					
DELX=1.0					
IF(M1.EQ,M2)DELX=DXA/0.025					

	MAG3	-	EFN	SOURCE STATEMENT	-	IFN(S)	-
				IF(N1.EQ. N2)DELZ=DZA/0/025			
				IF(M.EQ. M1)DELX=EM1-50.0-X1/0.025			
				IF(M.EQ. M2)DELX=X2/0.025+51.-EM2			
				IF(N.EQ. N1)DELZ=EN1-50.0-Z1/0.025			
				IF(N.EQ. N2)DELZ=Z2/0.025+51.-EN2			
				F=DELX*DELZ			
				FL(M, N)=FL(M, N)+F*CU(I)			
20				CONTINUE			
				DO 30 M=M1, M2			
30				WRITE(6, 400)(M, N, FL(M, N), N=N1, N2)			
400				FORMAT(IH 5(2I5, E15. 6))			
10				CONTINUE			
				DO 40 M=1, 100			
				DO 40 N=1, 100			
				IF(FL(M, N).GT. 10.E-WRITE(6, 400)M, N, FL(M, N)			
40				CONTINUE			
				WRITE(6, 600)			
600				FORMAT(1H12X2HAA4X3HPHA7X2HDQ8X2HXA4X2HZA3X3HDXA3X3HDXA4X3HA2A4X3H			
				1TH66X2HOM8X2HCU8X2HEM4X2HEN7X3HOM17X1HL)			
				WRITE(6, 700)(AA1(I), PHA(I), DQ(I), XA(I), ZA(I), DXA(I), DZA(I), A2A(I), T			
				1H1A(I), OM(I), CU(I), EM(I), EN(I), OM1(I), L(I), I=1, IMAX, 2)			
700				FORMAT(IH 2F6.1, 1PE14.5, OP4F6.3, 2F6.1, E13.3, F10.5, 2F6.1, E13.13.3, I6)			
				GO TO 1			
				END			